

## TUTORIAL REVIEW

# Anisotropic metal nanoparticles for surface enhanced Raman scattering

Javier Reguera,<sup>abc</sup> Judith Langer,<sup>ab</sup> Dorleta Jiménez de Aberasturi<sup>ab</sup> and Luis M. Liz-Marzán<sup>id\*abc</sup>

The optimization of the enhancement of Raman scattering by plasmonic effects is largely determined by the properties of the enhancing substrates. The main parameters behind this effect are related to the morphology of plasmonic nanoparticles and their relative distribution within the substrate. We focus this *tutorial review* on the effects of nanoparticle morphology, for the particular case of anisotropic metal nanoparticles. Anisotropy in silver and gold nanoparticles offers the possibility to tailor their plasmonic properties and intrinsic electromagnetic "hotspots". We describe the effect of varying particle size and shape on the SERS signal, focusing on the most common anisotropic morphologies used for SERS. Especial emphasis is made on existing comparative studies that shed light on the effect of nanoparticle anisotropy on their enhancement capabilities. We aim at providing a general perspective toward understanding the general key factors and highlighting the difficulty in quantitatively determining SERS performance.

## Key learning points

- Some fundamentals to understand SERS
- Importance of anisotropy toward SERS detection
- The most relevant anisotropic gold and silver nanoparticles in SERS
- Effects of shape and morphology on SERS (comparative studies)
- Key factors for SERS enhancement

## 1. Introduction

Noble metal nanoparticles (NPs) display a rich plasmonic behavior, which can be tuned *via* variations in the size and shape of the particles (ref. 1, 2 and references therein). Engineering of plasmon resonances in metal NPs is of great interest toward applications in very diverse fields. Sensing, light- and energy-harvesting, optoelectronics, biomedicine, and catalysis, are some of the most prominent examples. Among all metals, NPs made of silver (Ag) and gold (Au) play a central role in plasmonics as their resonances occur in the visible and infrared (IR) range of the electromagnetic spectrum, rendering them suitable for many applications. A large number of simple chemical methods have been developed for large scale production of NPs made of

these two metals, featuring low polydispersity, chemical inertness, bio-compatibility, and easy functionalization, so that they offer great potential in biological, biochemical and biomedical diagnostics, both *in vitro* and *in vivo*. A classical example is the use of spherical Au NPs in flow immunoassays, such as home pregnancy tests.

Engineering anisotropy in metal NPs has proven to be an extremely powerful tool for plasmon resonance tuning. Plasmon resonances in spheres can span a relatively small wavelength range (few tens of nm) by varying NP diameter, whereas shape anisotropy provides an additional degree of freedom that allows controlling plasmon resonance wavelengths, ranging from the visible through the mid IR, by varying the aspect ratio (AR) of the NPs. This is of high relevance in various sensing techniques, among which surface enhanced Raman scattering (SERS) is one of the most prominent examples. Raman scattering, which is based on inelastic light scattering upon vibrational excitation of molecules and materials is an extremely inefficient process with *ca.* one photon out of  $10^7$  being inelastically scattered. This drawback can however be overcome when the molecules are

<sup>a</sup> CIC biomaGUNE, Paseo de Miramón 182, 20014 Donostia-San Sebastián, Spain.  
E-mail: lizmarzan@cicbiomagune.es

<sup>b</sup> Biomedical Research Networking Center in Bioengineering Biomaterials and Nanomedicine, Ciber-BBN, 20014 Donostia-San Sebastián, Spain

<sup>c</sup> Ikerbasque, Basque Foundation for Science, 48013 Bilbao, Spain

located near a rough metal surface or metal NPs, which results in a boost of Raman scattering, in a process commonly known as SERS. Since its discovery in 1973,<sup>3</sup> the interest on SERS spectroscopy has increased tremendously, in turn pushing a fast technical development of high-end setups (with highly focused laser beams, efficient filters, highly sensitive detectors, etc.) as well as robust, potent and portable instruments. SERS spectroscopy has become an attractive technique for ultrasensitive detection, identification and, sometimes, quantification of a broad range of molecules.

A wide variety of anisotropic NPs have been developed with high potential for use in SERS sensing and imaging. Opposite to spherical NPs, aggregation is not required to generate

hotspots and plasmonic tunability can be readily obtained. In this tutorial, we review recent research on the use of the most common anisotropic Ag and Au NP morphologies toward SERS. We focus on the intrinsic shape-dependent SERS performance of anisotropic NPs, highlighting comparative and systematic SERS studies on NPs, mainly in solution. The article is organized as follows: in Section 2, we give a basic theoretical introduction to the optical properties of NPs and the SERS effect, as well as the relevant experimental techniques included in this report. In Sections 3–6 we present the most common anisotropic NP shapes, namely nanorods, nanotriangles, nanocubes and nanostars. Section 7 is dedicated to more complex structures that can offer additional advantages. After a short introduction of



**Javier Reguera**

*Javier Reguera is an Ikerbasque research fellow at CIC Biomagune in San Sebastián (Spain). He received a bachelor degree in Physics and a PhD in Materials Science (2008) at the University of Valladolid (Spain). He was a Fulbright fellow at Massachusetts Institute of Technology (USA) 2009–2011, and a postdoctoral scientist at École Polytechnique Fédérale de Lausanne (Switzerland) 2011–2014. He joined CIC BiomaGUNE (Spain) in 2014*

*where his research interests include the synthesis of patchy and multicomponent nanomaterials, self-assembly at interfaces and applications in nanobiomedicine, imaging and sensing.*



**Judith Langer**

*Judith Langer obtained a PhD from Freie Universität Berlin in 2003 for work on low-energy electron attachment on clusters in supersonic beams, under the supervision of Prof. Eugen Illenberger. After postdoctoral research at the Institute of Materials Science of Barcelona (ICMAB), the Institute of Physical Chemistry at Freie Universität Berlin and the Institute of Optic and Atomic Physics at Technische Universität Berlin, working on*

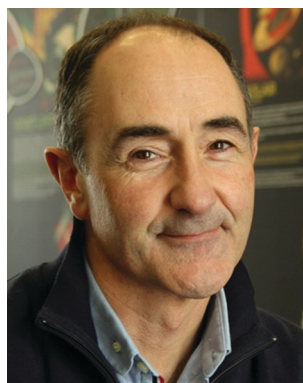
*different materials and infrared (multiphoton) dissociation, she joined the Bionanoplasmonics Lab at CIC biomaGUNE headed by Prof. Luis Liz-Marzán in 2012. Her current research focuses on the application of plasmonic nanoparticles for bioimaging and sensing by SERS.*



**Dorleta Jiménez de Aberasturi**

*Dorleta Jimenez de Aberasturi graduated from the University of the Basque Country (UPV/EHU) in 2006. In 2013, she received her PhD entitled “Design of multifunctional colloidal particles with ion selective ligands” in cotutelle between the UPV/EHU and Philipps University of Marburg under the joint supervision of Prof. Dr Teófilo Rojo, Dr Idoia Ruiz de Larramendi and Prof. Dr Wolfgang Parak, obtaining the special doctoral award. Since 2014 she has worked in the group of Prof. Liz-Marzán at*

*CICbiomaGUNE. Her current research involves plasmonic nanoparticle synthesis, assembly and their functionalization for biosensing and imaging.*



**Luis M. Liz-Marzán**

*Luis Liz-Marzán is Ikerbasque Professor and Scientific Director of CIC biomaGUNE, in San Sebastián (Spain), since September 2012. He graduated in chemistry from the University of Santiago de Compostela, was postdoc at Utrecht University and Professor at the University of Vigo (1995–2012). He has been Invited Professor at several universities and research centers worldwide and received numerous research awards. His major research activity*

*is devoted to understand the growth mechanisms of metal nanocrystals, to tailor their surface chemistry and direct self-assembly. He also works on the design of biomedical applications based on the plasmonic properties of well-defined metal nanoparticles and nanostructures.*

each shape class, we briefly describe the optical properties, and discuss some recent works where the morphology-dependent SERS performance can be appreciated.

## 2. Brief theoretical aspects

### 2.1. Plasmonics

The unusual optical properties of metal NPs are related to the presence of strong plasmon resonances in the visible and near-IR (NIR) ranges of the electromagnetic spectrum. Plasmon resonances exist in all metals and refer to the excitation of coherent, collective oscillations of delocalized electrons in the conduction band by an external electromagnetic (EM) field as the driving force. Similar to the illustrative picture of a driven oscillator in classical mechanics, here the frequency of the incident light wave is in resonance with the characteristic frequency of the free electrons in the metal (plasma frequency) driving the electron movement with the amplitude of the light field. In metal NPs, plasmon resonances exist at the interface between the metal

and a dielectric and are laterally confined due to the nanoscale dimensions of the NPs. They are thus termed localized surface plasmon resonances (LSPRs). The LSPR wavelength depends on the dielectric function of both the metal  $\epsilon$  and the surrounding medium  $\epsilon_m$ , the NP morphology and the number of delocalized electrons.

As the excitation wavelength is typically much larger than the NP dimension ( $\lambda \gg r$ ), LSPR modes possess dominantly a dipolar character. In the case of a sphere (isotropic), a dipole is induced along the electric field vector of the light wave. The corresponding moment  $\mu_{\text{ind}}$  is determined by the incoming EM field  $E_0(\omega_0)$  and the polarizability  $\alpha$  (the degree on how easily the electron cloud can be displaced) of the NP ( $\mu_{\text{ind}} = \alpha E_0(\omega_0)$ ). The situation in anisotropic NPs becomes more complex. As  $\alpha$  is a tensor, its components can differ along the three main axes and several dipole modes can exist depending on the NP symmetry and orientation. This is exemplarily shown for nanorods (Fig. 1A), which can accommodate two different dipolar LSPRs, namely the transverse mode (electron oscillation perpendicular to the NR main axis) and the longitudinal mode (electron oscillation

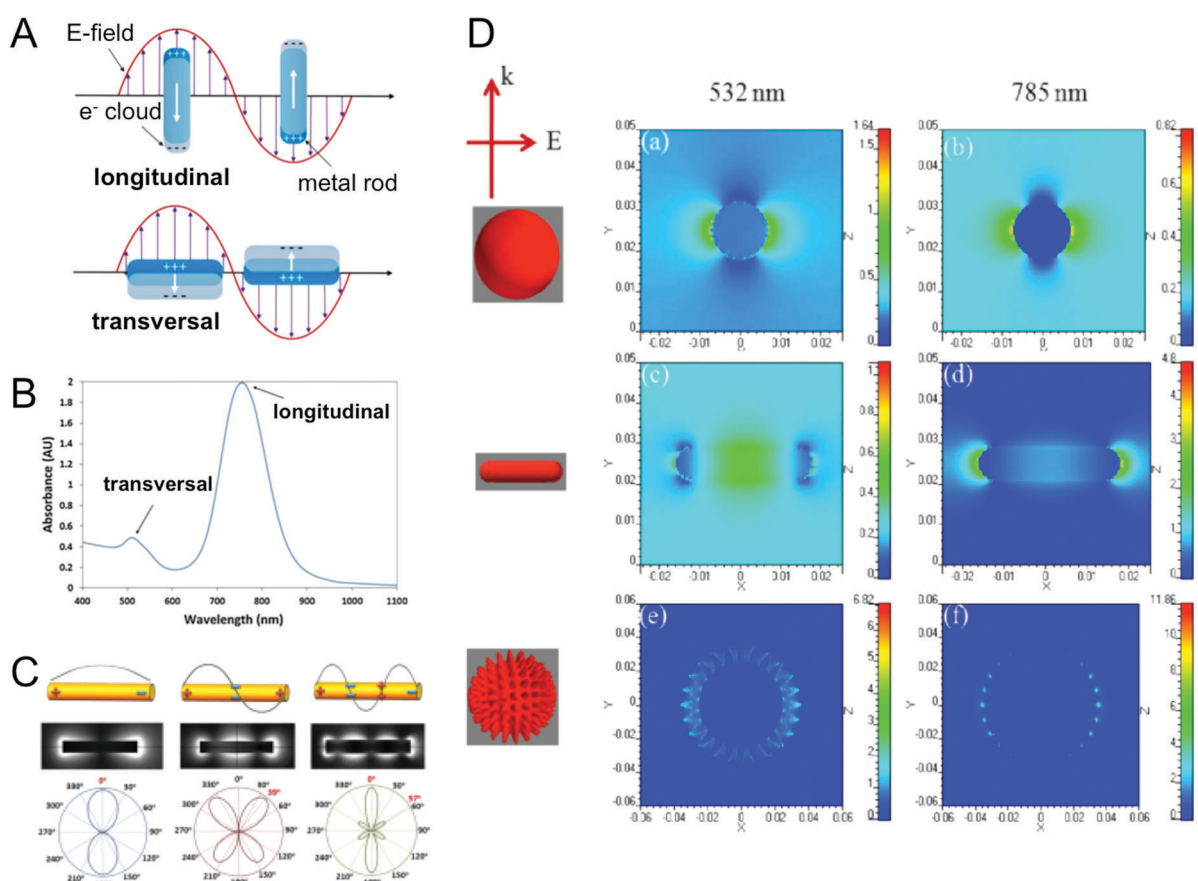


**Fig. 1** (A) Orientation-dependence of dipolar LSPRs in NRs, longitudinal (top) and transverse (bottom) mode.<sup>4</sup> (B) UV-Vis spectrum of AuNRs showing the position and intensity of transverse and longitudinal LSPR modes.<sup>4</sup> (C) Illustration of the quadrupolar (center) and hexapolar (right) character of LSPRs in long NRs compared to the dipole (left), and corresponding EM field distributions. With increasing pole order high-field areas along the rod axis appear.<sup>5</sup> (D) EM field distributions and intensities for nanorods and nanostars, compared to spherical NPs, upon excitation at two different wavelengths indicating that the highest near-field is generated at the LSPR wavelength and focused at the sharp tips of anisotropic NPs (here at 785 nm). Note that the LSPR wavelength for an Au sphere is around 520 nm.<sup>6</sup> Reproduced with permission of: ref. 4 CC-BY, 2016 Intech; ref. 5. CC-BY 2012 SpringerOpen; ref. 6 Copyright © 2012 IOP Publishing.

parallel to the main axis). The wavelength of the longitudinal mode is here significantly red-shifted with respect to that of the transverse mode, due to its higher  $\alpha$  (Fig. 1B).

Upon resonant excitation of strong LSPRs, a greatly enhanced local EM field (near-field)  $E_{\text{loc}}(\omega_0)$  relative to the incident excitation field  $E_0(\omega_0)$  is generated at the NP surface. This near-field in turn couples to the incident field and re-emits radiation with the same wavelength (resonant scattering). As the scattering cross section scales with  $\alpha^2$  also the near-field strongly increases for anisotropic NPs due to higher  $\alpha$ , as compared to spheres (Fig. 1D). Elongated NPs or those with edges and corners, such as nanorods, nanocubes, and nanotriangles, thus generate strong near-fields concentrated at vertices. Trapping the oscillating metal charges in highly confined spaces, *e.g.* at the sharp tips of nanostars, can lead to even stronger near-field enhancements. These areas of locally high near-field are known as *intrinsic* hotspots. A different type, *extrinsic* hotspots, are generated when NPs are positioned at very short distances (1–10 nm) or on top a solid support. The coupling of plasmon modes between individual NPs or between a NP and a flat metal surface leads to new modes with highly localized, intense EM fields at the narrow gaps within the junctions.

Fig. 1D also shows that, when the NP is irradiated under off-resonance conditions, the resulting near-field is significantly lower and less confined than under resonance conditions. Resonant scattering becomes generally more dominant over absorption as the size of the NP increases. Note that absorption as well as resonant scattering by NPs, are both strongly increased at the LSPR wavelength. Therefore, the measurement of extinction (the sum of absorption and scattering) in the far-field fairly mirrors the LSPR excitation and the resulting near-field spectrum. In large NPs or those with high AR, LSPRs with multipolar character can also be excited, such as longitudinal quadrupolar and hexapolar modes in long NRs. These modes differ in near-field strength and distribution. Apart from the two hotspots at the tips, additional high-field nodes form along the main axis, as shown in Fig. 1C.

The efficiency of LSPR excitation (and hence the near-field intensity) is largely influenced by the dielectric constant of the metal  $\epsilon(\omega)$ , defined as a function of the angular frequency of the applied field  $\omega$ :  $\epsilon(\omega) = \epsilon'(\omega) + i\epsilon''(\omega)$ . The real part  $\epsilon'(\omega)$  reflects how strongly the material is polarized upon exposure to an external EM field, while the imaginary part  $\epsilon''(\omega)$  represents

how strongly the LSPR and near-field are damped, *e.g.* due to intraband or interband transitions, electron–phonon collisions and electron scattering with the surface. Ag exhibits the lowest losses in the visible and NIR frequency ranges, whereas Au shows significant plasmon damping at wavelengths below 600 nm. These dielectric properties render Ag the material of choice for applications in the visible (350–650 nm). In practice however, the use of Ag NPs is limited due to higher reactivity and susceptibility to oxidation. On the other hand, Au is an eminently inert material (though also more expensive), so that the choice of material ultimately depends on the framework requirements for each specific application.

## 2.2. Surface enhanced Raman scattering

In Raman scattering, molecules interact with an incident EM field  $E_0(\omega_0)$ , *e.g.* from an intense laser beam. Similar to plasmons in NPs, depending on the polarizability of the molecule, an oscillating dipole is induced exciting the molecule into a virtual state. In the classical picture, scattering can be described by the modulation of incident field through a molecule vibrating with an eigenfrequency  $\omega_{\text{vib}}$  by irradiating an EM field with shifted frequency  $E_0(\omega_{\text{R}})$ , as schematically shown in Fig. 2 (top). Raman scattering can be dramatically improved when the molecule of interest is close to a metallic surface or preferentially in contact with the same. As the EM field strength attenuates as  $1/r^2$ , a typical value  $r$  for the distance between molecule and NP surface ranges between 0–10 nm. The presence of the plasmonic near-field at the NP surface upon LSPR excitation  $E_{\text{loc}}(\omega_0)$  increases  $\alpha$  of the molecule (or more correctly of the molecule-NP ensemble) by 1 to 3 orders of magnitude compared to free molecules, due to mutual excitation between induced dipole in the molecule and induced dipole in the NP. In other words, NP and molecule scatter the impinging field whereupon the NP irradiates a locally enhanced EM field, which can be re-scattered by the molecule leading to enhanced Raman scattering. In turn, the molecule irradiates the Raman-scattered field, which is then re-scattered by the NP upon LSPR excitation and re-emission of an enhanced near-field  $E_{\text{loc}}(\omega_{\text{R}})$  (with shifted frequency). This situation is pictured in Fig. 2 (bottom). The SERS intensity  $I_{\text{SERS}}$  thus depends on both incident (incoming)  $E_0(\omega_0)$  and scattered (outgoing) fields  $E_{\text{loc}}(\omega_{\text{R}})$ , and SERS enhancement is achieved when incoming and outgoing fields are in resonance with the LSPR of the NP. As molecular vibration frequencies  $\omega_{\text{vib}}$  are small

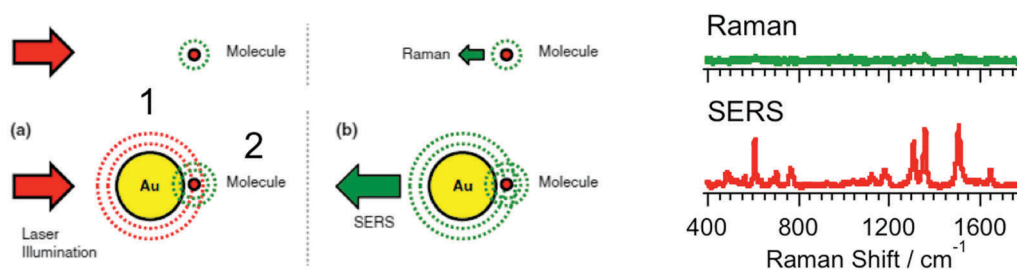


Fig. 2 Basic SERS electromagnetic mechanism. The AuNP (1) enhances both (a) the incident laser field and (b) the scattered field, greatly boosting the Raman scattered signal from the nearby molecule (2). Reproduced with permission of ref. 7. Copyright © 2012 IOP Publishing. This effect is exemplarily shown by experimentally measured Raman and SERS spectra of rhodamine 6G (right-hand figure, measured onto assembled Au nanostars substrate).

compared to the excitation frequency  $\omega_0$ , the shift ( $\omega_0 - \omega_{\text{vib}} = \omega_{\text{R}} \approx \omega_0$ ) of the outgoing field is also small and the enhancement factor (EF) can be approximated to the fourth power of the local EM field enhancement at NP surface  $\text{EF} = I_{\text{SERS}}/I_{\text{Raman}} = (E_{\text{loc}}(\omega_0))^2(E_{\text{loc}}(\omega_{\text{R}}))^2/(E_0(\omega_0))^2(E_0(\omega_{\text{R}}))^2 \approx (E_{\text{loc}}(\omega_0)/E_0(\omega_0))^4$ . This effect can be illustrated by a simple numerical example. Even a moderate enhancement of plasmon-supported EM field with a factor 10 would increase the intensity by  $10^4$ , but with a field enhancement of 100 the intensity would rise by  $10^8$ . In the context of practical applications, this conclusion has an important impact on how NPs should be tailored to maximize the EM field enhancement and hence the SERS output. Here, the NP morphology occupies a key position. The above described mechanism of SERS is known as *electromagnetic* mechanism. Note that it requires the presence of a molecule but is not dependent on its nature.

If the molecule binds to the NP surface, the electronic interaction between molecular orbital and NP conduction band can give rise to new charge-transfer resonances, which can couple to vibrational states of the (adsorbed) molecule. This can give rise to a significant reallocation of electron density within the molecule and a change of  $\alpha$  during the vibrational motion leading to additional SERS enhancement with EFs of  $10^1$ – $10^3$ . This effect, known as *chemical mechanism*, is generally much smaller than the electromagnetic effect but can improve the SERS sensitivity when charge-transfer resonances, LSPR and incident excitation wavelength are matched. If electronic resonances of the molecule or rather the adsorbate-NP complex are involved, the Raman cross section and hence the signal intensity further increase due to surface enhanced resonant Raman scattering (SERRS).

To evaluate the performance of different NP morphologies and structures, their SERS response must be compared by using an adequate reference. To date, the most established method to evaluate the SERS efficiency is the determination of EF. The EF is defined as the ratio between the intensities of SERS ( $I_{\text{SERS}}$ ) and ordinary Raman ( $I_{\text{RS}}$ ) for a given molecular mode, both measured under the same experimental conditions. The intensities  $I_{\text{SERS}}$  and

$I_{\text{RS}}$  must be weighed by the numbers of molecules involved in RS ( $N_{\text{RS}}$ ) and SERS ( $N_{\text{SERS}}$ ). Estimation of EF then results in:  $\text{EF} = I_{\text{SERS}}N_{\text{RS}}/I_{\text{RS}}N_{\text{SERS}}$ . Measuring EFs from colloidal solutions leads to the determination of so-called analytical EF. Indeed, they are typically much smaller compared to those on dry surfaces but instead we record a statistically relevant number of molecules. Thus, the obtained results are more reproducible than for single- or few-molecule events whose values can strongly scatter from event to event. For a detailed understanding of the theory, practical advantages and drawbacks of alternative approaches, the reader is directed to the comprehensive review by Le Ru and Etchegoin.<sup>8</sup>

In order to facilitate the understanding of the characterization methods used for selected examples of plasmonic nanoparticles and adsorbed molecules, Table 1 summarizes the most common experimental and theoretical methods that are relevant within this tutorial.

### 3. Nanorods

Nanorods (NRs) and nanowires (NWs) are nanostructures where one dimension is longer than the other two (ref. 9 and references therein). The term nanorods is commonly referred to relatively short elongated particles (length < 100 nm), while nanowires are longer, not always perfectly straight, typically with AR above 10 and length up to 5  $\mu\text{m}$ . NWs are known since around 1960, when the vapor–liquid–solid approach was developed. During the 1990’s electrochemical and photochemical methods were used for the synthesis of Au and Ag NRs and NWs, but it was not until the early 21st century that the so called seed-mediated growth was developed, which has become the most popular approach.<sup>9</sup> This method comprises the synthesis of small metal NPs, “seeds”, which are then overgrown into larger particles with different shapes by reduction of a metal salt in the presence of a “shape-directing” surfactant. Thus, nucleation and growth are temporally separated, leading to uniformity and precise control

**Table 1** Experimental and theoretical methods for the characterization of NPs and molecules relevant to this tutorial

Experimental methods	Characterization
<ul style="list-style-type: none"> <li>• Ultraviolet-visible (UV-Vis) spectroscopy</li> <li>• Dark-field (DF) optical microspectroscopy</li> <li>• Scanning electron microscopy (SEM)</li> <li>• Transmission electron microscopy (TEM)</li> <li>• Scanning TEM (STEM)</li> <li>• Electron energy loss spectroscopy (EELS)</li> <li>• Energy dispersive X ray (EDX) absorption</li> <li>• Annular dark field (ADF) detection</li> <li>• High-angle ADF (HAADF)</li> <li>• Cathodoluminescence (CL)</li> <li>• Surface enhanced Raman scattering (SERS)</li> </ul>	<ul style="list-style-type: none"> <li>Extinction, LSPR and molecular resonance wavelength (or frequency, energy)</li> <li>Scattering, LSPR wavelength (or frequency, energy)</li> <li>Morphology of NPs</li> <li>Morphology and crystallinity of NPs</li> <li>Morphology, crystallinity and orientation of NPs</li> <li>LSPR mapping: near-field (or local electromagnetic field) intensity and spatial distribution</li> <li>Elemental analysis: distribution and chemical composition</li> <li>Scattered electron mapping</li> <li>Incoherently scattered electrons mapping (z-contrast)</li> <li>LSPR mapping</li> <li>Chemical mapping: structure, orientation, interaction of molecules with metal surface, relative near-field (or local electromagnetic field) intensity and distribution (not relevant in this review)</li> </ul>
Theoretical simulations <ul style="list-style-type: none"> <li>• Discrete dipole approximation (DDA)</li> <li>• Finite-difference time domain (FDTD)</li> <li>• Boundary element method (BEM)</li> <li>• Surface-integral equations discretized by the method of moments (SIE-MoM)</li> </ul>	<ul style="list-style-type: none"> <li>LSPR modes, near-field (or local electromagnetic field) intensity and distribution,</li> <li>EELS, CL, SERS</li> </ul>

over particle size and aspect ratio. AgNRs and AgNWs were successfully prepared in 2001 by Murphy *et al.*, by reducing silver nitrate ( $\text{AgNO}_3$ ) with ascorbic acid in the presence of Ag seeds.<sup>10</sup> The use of cetyltrimethylammonium bromide (CTAB) as surfactant and different amounts of NaOH promoted the formation of NRs at high NaOH concentrations, or NWs at low concentrations. In the case of Au, high-yield (>90%) colloidal synthesis of monodispersed single crystal AuNRs was introduced by Nikoobakht and El-Sayed in 2003.<sup>11</sup> Since then, several approaches have been reported, further improving quality and yield, reaching values higher than 99% shape yield.<sup>12</sup> The addition of low amounts of  $\text{Ag}^+$  ions was essential to obtain high NR yield in this approach, whereas Ag-free NR growth leads to mixtures of pentatwinned NRs, spheres and other shapes. Very recently, yields above 85% have also been obtained for pentatwinned NRs, by optimization of pentatwinned seeds.<sup>13</sup>

LSPR wavelengths in NRs can be readily tuned, by simply varying the aspect ratio (Fig. 3). Typical UV-Vis spectra feature two plasmon bands, corresponding to transverse and longitudinal modes. Whereas the intensity of the transverse LSPR band is relatively low and nearly independent of the AR, the longitudinal LSPR is much more intense and strongly dependent on AR (Fig. 3B).<sup>14</sup> Interestingly, the plasmon modes in NRs give rise to regions with intense EM fields, in the proximity of the NP. This is illustrated in Fig. 4, which shows theoretical (DDA) and experimental (EELS) near-field maps for pure AuNRs and AgNRs.<sup>15,16</sup> DDA simulations for AuNRs (Fig. 4A) have shown the equivalence between plasmon excitation by light (extinction cross section in Fig. 4A(I)) and by electrons (loss probability in Fig. 4A(II)).

Both calculations indicate high EM field enhancement at the NR tips (hotspots) under longitudinal excitation, but moderate field enhancement on the NR lateral sides for transverse excitation. Similar results were obtained from EELS experiments (Fig. 4A(III)) and also for AgNRs. Fig. 4B(III) shows the localized field enhancement at NR tips for the dipolar longitudinal mode (top image). Furthermore, at higher energies new multipolar modes appear (lower images), with enhancement at intermediate nodes. Although these multipolar modes can in principle be used for SERS, the highest near-field intensity produced at the longitudinal dipolar mode with intense hotspots at the tips, still render this mode the preferred choice.

NRs are undoubtedly the most widely used anisotropic nanoparticles as SERS substrates. Tailoring the LSPR relative to the laser excitation wavelength, to produce an on-resonance measurement, is one of the most important keys to achieve a high Raman enhancement. This has been confirmed by a size-dependent SERS study on AgNRs and AuNRs with AR ranging from 1.7 to 16 and under 633 nm excitation.<sup>17</sup> The authors demonstrated three aspects: (1) AgNRs generate higher EFs than AuNRs at 633 nm. (2) The EF for AgNRs increases with increasing AR whereas for AuNRs the EF decreases. This is explained by the LSPR red-shift with increasing AR driving the resonance towards excitation wavelength in case of Ag and away from excitation wavelength in case of Au. (3) Although nanorods with LSPRs not matching the excitation wavelength (off-resonance) can show relatively high EFs ( $10^4$ – $10^6$ ), 1–2 orders of magnitude greater enhancements are estimated for NRs on-resonance. El-Sayed's group compared SERS on AuNRs vs. spherical AuNPs

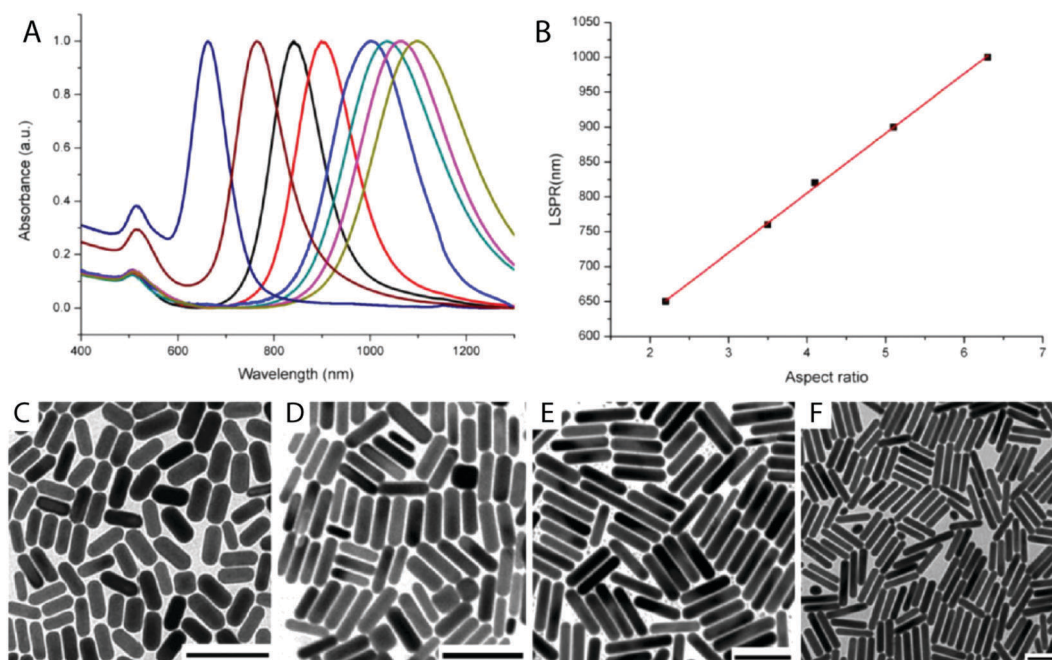


**Fig. 3** Characterization of gold nanorods. (A) Representative UV-Vis-NIR spectra of AuNRs with longitudinal LSPR bands at 650 nm, 760 nm, 840 nm, 900 nm, 1000 nm, 1036 nm, 1060 nm and 1100 nm (from left to right). (B) Relationship between longitudinal LSPR and AR (measured from TEM images). (C–F) Representative TEM images of AuNRs with longitudinal LSPR at (C) 650 nm, (D) 760 nm, (E) 920 nm, and (F) 1000 nm. Scale bars: 100 nm. Reproduced with permission of ref. 14. CC-BY, 2015 Ivyspring.

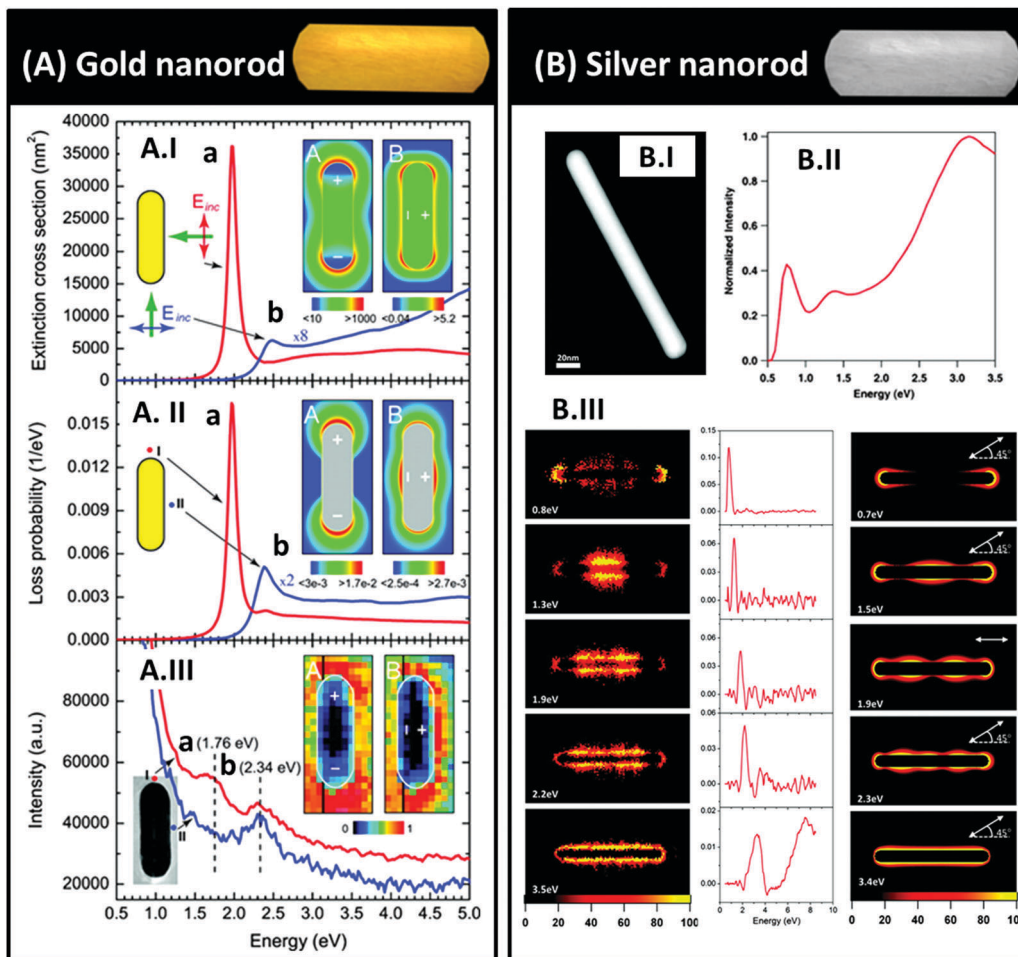


Fig. 4 (A) AuNRs: comparison of excitation with light vs. electrons, of the NR longitudinal and transverse LSPR modes. (A.I) Calculated extinction cross section for an individual NR (diameter/length, 27/85 nm), using parallel (red curve) or perpendicular (blue curve) incident light-electric field to the rod axis, leading to excitation of bright LSPR modes. Inset: Calculated near-field maps for both modes. The positive and negative signs denote the induced charge oscillation patterns of the modes. (A.II) Calculated electron energy loss probability for locations I (red curve) and II (blue curve) of the electron beam relative to the NR under grazing incidence. The loss probability is given per incoming electron and per electronvolt for a given lost energy. Inset: Calculated EELS excitation-intensity maps. (A.III) Experimental counterpart of (A.II). Inset: Measured EELS excitation-intensity maps for modes a and b. Color scale bar represents the linearly normalized image intensity.<sup>15</sup> (B) AgNRs: (B.I) electron microscopy (ADF) image of a high AR AgNR: length = 192 nm, diameter = 20 nm, AR = 9.6. (B.II) Summed electron energy loss spectrum (B.III) starting from the left column, multivariate statistical analysis (MVSA) score images and loading spectra interpreted as plasmon maps and energies, respectively. Right, DDA calculated electric field plots displaying the field generated by a plane wave optical excitation at the energies and polarizations given on each panel.<sup>16</sup> Reproduced with permission of ref. 15 and 16 Copyright © 2009, 2011 American Chemical Society.

under off-resonance conditions.<sup>18</sup> Interestingly, the measured EFs ( $10^4$ – $10^5$ ) were two orders of magnitude higher than expected from the electromagnetic mechanism, indicating significant chemical enhancement. The SERS activity was higher for AuNRs than for AuNPs, which was explained by the presence of more reactive facets in AuNRs. The same group recently reported a comparative study between AgNRs and AuNRs with comparable ARs and longitudinal LSPR peak position (Fig. 5).<sup>19</sup> The results confirmed that AgNRs are more efficient than AuNRs: EF values of 0.1 to  $2.0 \times 10^{14}$  for AgNRs vs. 0.3 to  $2.2 \times 10^{12}$  for AuNRs were reported. This was attributed to the higher plasmon field intensity at the tips of AgNRs as observed in DDA simulations (Fig. 5B–E), and to higher Rayleigh scattering for AuNRs. The extraordinarily high values of EF differ from other works on NRs,

which highlights the difficulties to compare results obtained in different labs.

It should be noted that, apart from LSPR position and composition, other factors can also affect SERS performance. A recent comparative study showed that AuNRs with different sizes but equal LSPR wavelength provide different SERS under the same conditions (see Fig. 6).<sup>20</sup> It was found that larger NRs show stronger scattering intensity but weaker SERS. The larger SERS signal at smaller sizes was attributed to a synergistic effect between the stronger lightning rod effect (charge concentration at the tips), and to the weaker radiation damping resulting in stronger local field enhancement. The same effect was observed when extrinsic hotspots were generated by formation of NR dimers with equal LSPR but different sizes. It should be noted

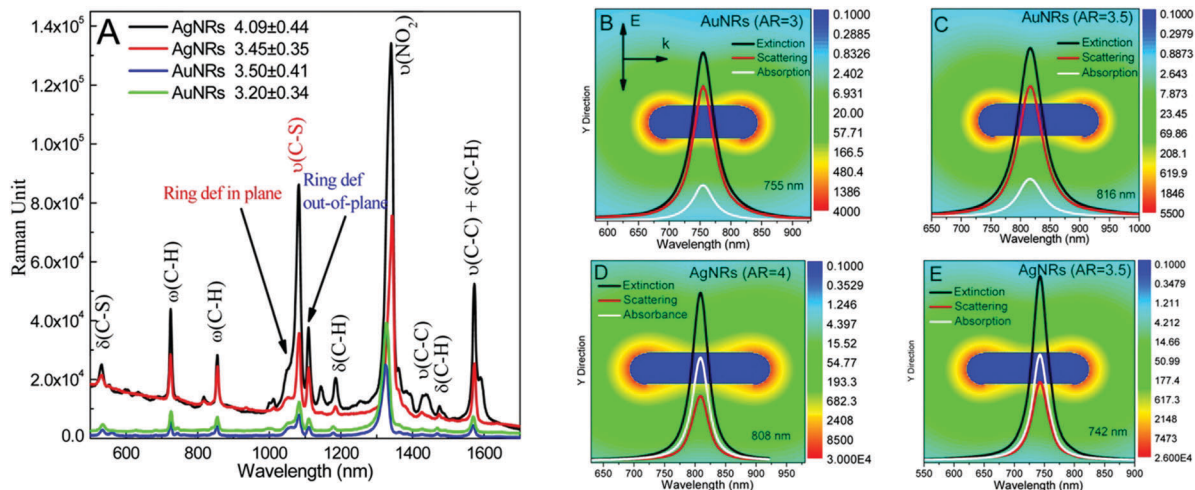


Fig. 5 (A) SERS of 4-nitrothiophenol adsorbed on the surface of AuNRs and AgNRs with similar ARs (AgNRs:  $3.45 \pm 0.35$  and  $4.09 \pm 0.44$ , AuNRs:  $3.20 \pm 0.34$  and  $3.50 \pm 0.41$ ) excited at 785 nm. Plasmon maps simulated by DDA for AuNRs and AgNRs of 22 nm diameter and different AR: (B) AuNRs, AR = 3, (C) AuNRs, AR = 3.5 (D) AgNRs, AR = 4, (E) AgNRs, AR = 3.5. Color code for the spectra in panels B–E: extinction (black), scattering (red), and absorption (white). Reproduced with permission of ref. 19. Copyright © 2013 American Chemical Society.

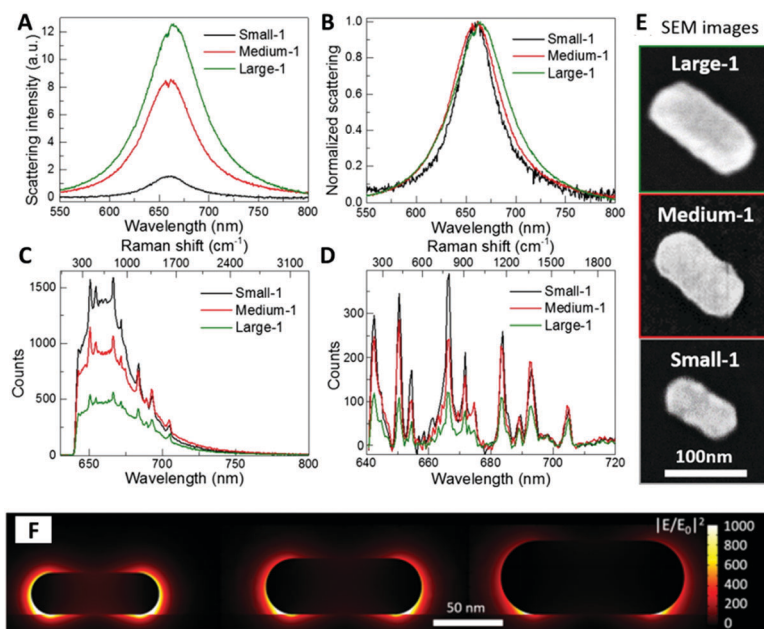


Fig. 6 (A) Single nanoparticle dark field scattering spectra of three AuNRs showing different scattering intensities. (B) Normalized DF spectra. (C) Single nanoparticle SERS spectra of malachite green isothiocyanate (MGITC) on the three AuNRs. (D) Background-subtracted SERS spectra. Both white light and laser polarizations were parallel to the nanorods. (E) Representative SEM images. (F) Simulated local electric field scattering cross section maps. Reproduced with permission ref. 20. Copyright © 2016 American Chemical Society.

that the employed NRs are larger and rougher than those usually obtained by wet chemistry methods.

When comparing the SERS efficiency of different NRs, special care should be taken to maintain similar experimental conditions. For example, NR concentration in the colloid is an important parameter when dense suspensions are used.<sup>21</sup> This could be of special importance in biological applications where a high variability of NP concentration exists (cell cytoplasm, endosomes, *etc.*). Murphy and co-workers showed, using concentrated AuNR solutions of different AR, that the effectively

measured SERS intensity can be attenuated by extinction of both the incident and scattered light during propagation (Fig. 7).<sup>21</sup> The maximum SERS signal (taking the number of Raman reporter molecules per Au NR into account) was obtained from NRs with plasmon resonances that are far blue-shifted from the excitation wavelength at 785 nm, since the intensity of on-resonance SERS was quenched, and in striking contrast to the electromagnetic enhancement mechanism. On the basis of this result, the authors developed a model for extinction-corrected EFs which explained the maximum EF at AR = 2.75 instead of 4 as expected from the

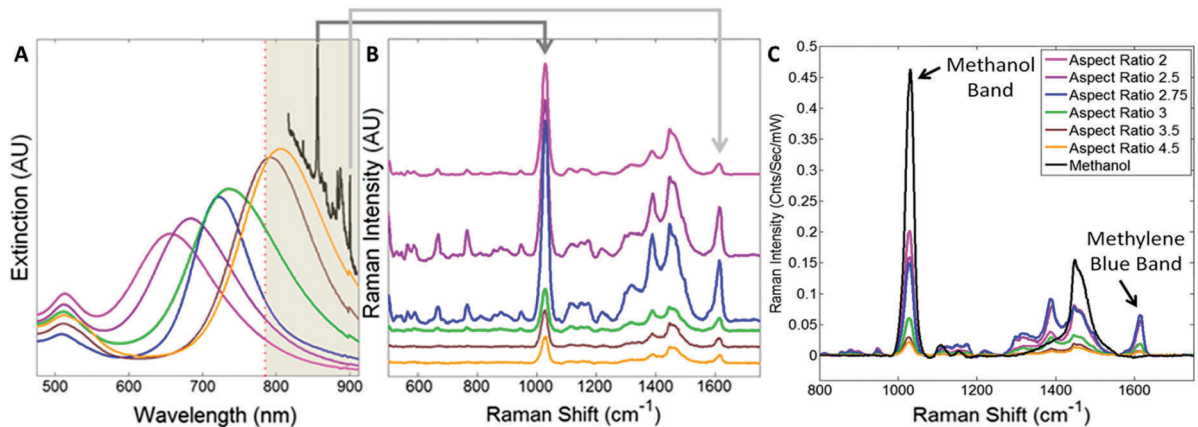


Fig. 7 (A) Extinction spectra for AuNRs of different AR (pink: 2; purple: 2.5; blue: 2.75; green: 3; brown: 3.5; orange: 4.5), normalized to concentration. The Raman excitation wavelength is indicated by a red-dotted vertical line and the Raman spectrum in black. (B) SERS spectrum of methylene blue (MB) on the various AuNRs bearing a polyelectrolyte layer, normalized for AuNR and reporter molecule concentrations. (C) Comparison of Raman spectra acquired from the suspensions bearing polyelectrolyte layers plus MB reporter in methanol. The variation in Raman intensity for the methanol bands is illustrated by the peak at  $1030\text{ cm}^{-1}$ , which varies as a function of AR. AuNR suspensions are normalized for concentration and the number of reporter molecules per AuNR. Reproduced with permission of ref. 21 Copyright © 2013 American Chemical Society.

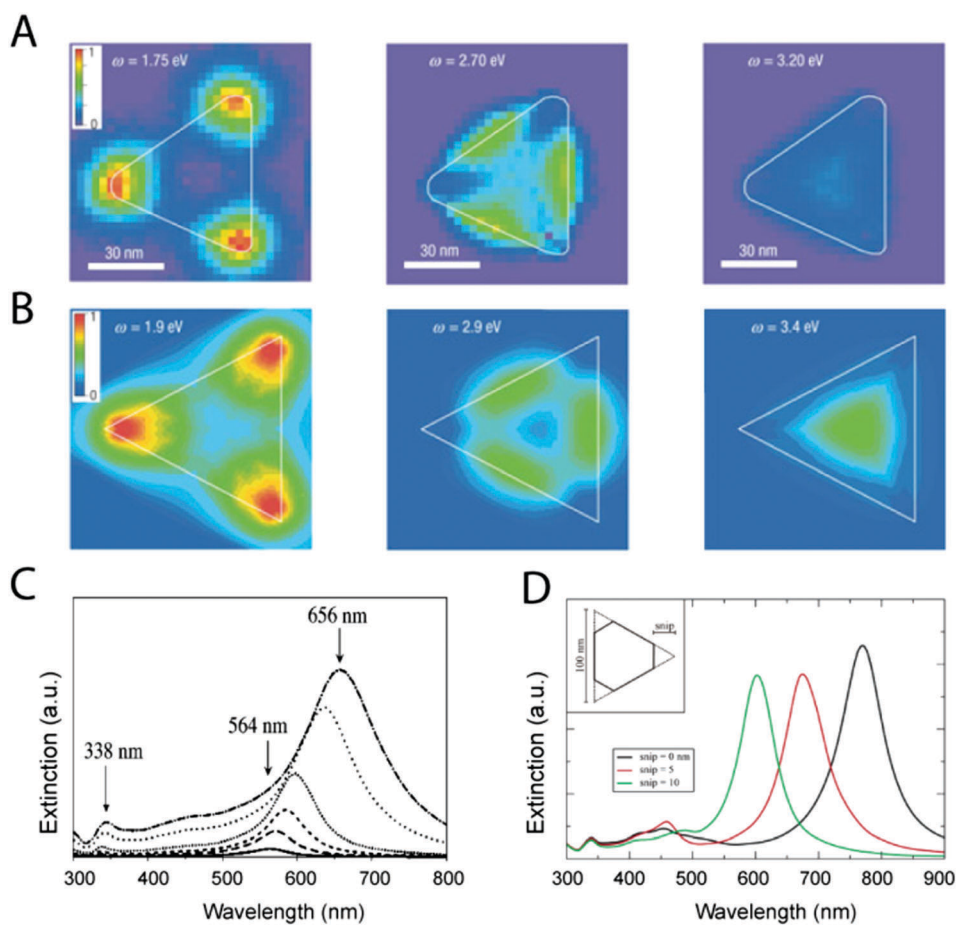


Fig. 8 (A) EELS maps of an Ag NT at different energies, showing the in-plane dipolar and quadrupolar plasmon modes.<sup>22</sup> (B) BEM simulation of EELS for the same NT.<sup>22</sup> (C) Extinction spectra of Ag NTs at different sizes from 20 to 128 nm (DDA simulations).<sup>24</sup> (D) Extinction spectra of truncated Ag NTs at different snip sizes (DDA simulations).<sup>1</sup> Reproduced with permission: ref. 22 Copyright © 2007 Macmillan Publishers Ltd; ref. 1 and 24 Copyright © 2003, 2007 American Chemical Society.

electromagnetic mechanism. Two spectral features were considered: the Raman band from methanol at  $1030\text{ cm}^{-1}$  which should only decrease from extinction of the Raman excitation wavelength (not enhanced by AuNRs) and the Raman signal from methylene blue (MB) at  $1616\text{ cm}^{-1}$  which is affected by the LSPR position, in turn determined by the AR of AuNRs (Fig. 7B). Under such conditions, NRs with lower ARs are thus preferred to optimize the spectroscopic response. It is likely that such a drastic attenuation appears only when a critical concentration threshold is reached. This effect was not observed when SERS was measured from NRs deposited on solid substrates.

## 4. Nanoplates

Nanoplates are nanomaterials in which one of the dimensions is much smaller than the other two. Diverse names have been used in the literature to name them. For example, the term nanoprisms is not uncommon, since most nanoplates have a polygonal base, whereas the name nanodiscs is used for plates with a round base. For the specific case of triangular or hexagonal bases, they are also referred to as nanotriangles (NTs) and nanohexagons, respectively. We focus again on NTs made of Au or Ag, the most common choice for SERS studies. NTs are of high interest because of their inherent sharp corners and edges, which can confine EM fields and therefore exhibit strong enhancements. Fig. 8A shows high-resolution EELS maps of a single AgNT at different energies. EELS mapping evidences high EM field enhancement at the tips, corresponding to a dipolar plasmon mode, while other modes at higher energies present the highest enhancement at the edges and at the center of the NT.<sup>22</sup> These results were also confirmed by BEM simulations (Fig. 8B), with an excellent agreement between the in-plane dipole and quadrupole plasmon modes and the EELS mapping at the corresponding energies. Cathodoluminescence has also been used to map the plasmon modes of NTs, but while EELS can map radiative and nonradiative plasmon modes (bright and dark modes, respectively), CL maps only radiative modes, which allows a clear distinction between optical extinction and scattering by nanoparticles.<sup>23</sup> NTs present tunable plasmon resonances, the LSPR being readily selected by changing the AR (edge/thickness). For instance, an increase in AR produces a red-shift in the dipolar LSPR (Fig. 8C). Additionally, NTs may present different degrees of truncation, depending on the selected synthetic method and preparation conditions. Truncation can also be used to tune the dipolar LSPR, leading to a blue-shift in the spectrum as the snip size of the missing corner is increased (Fig. 8D).<sup>1,24</sup>

Therefore, the suitability of NTs as excellent SERS substrates is not only related to their ability to generate high EM field enhancement, but also to LSPR tunability, which can be conveniently adapted to the available excitation laser wavelength. Despite of this, the use of NTs for SERS has been scarce, as compared to NRs, mainly due to the synthetic difficulties to obtain them in high yield, as often other shapes (secondary products) are simultaneously obtained. Existing synthetic methods include light induced synthesis and wet chemistry methods, where surfactant

molecules such as polyvinylpyrrolidone (PVP), cetyltrimethyl ammonium chloride (CTAC) or CTAB, as well as halides (iodide usually) act as shape directing chemicals, guiding NP growth into plate-like morphologies. Recent advances in colloidal wet chemistry methods, and especially in post-synthesis purification steps, have succeeded in achieving high yields as well as improved monodispersity, thereby increasing their usability in SERS. Scarabelli *et al.* recently reported the synthesis of Au nanotriangles with sizes ranging from 60 up to 150 nm and yields above 50% that could be further increased up to 95% upon simple purification.<sup>25</sup> The obtained NTs were used as SERS substrates in solution to measure different dye molecules in concentrations as low as  $10^{-8}\text{ M}$  and EFs of  $10^5$  (Fig. 9).

It may be difficult to compare the SERS performance of different NTs, as small morphological changes can lead to significant LSPR variations and in turn to shift away from the selected SERS excitation wavelength. However, there is common agreement that sharp corners are extremely advantageous to obtain high SERS enhancement. As an example, Yang *et al.* showed that AgNTs with sharp corners produce larger enhancement than rounded NTs (Fig. 10).<sup>26</sup> Interestingly, they also found that wavy edges generated a further enhancement with respect to straight ones, which is likely due to LSPR band broadening, so that a

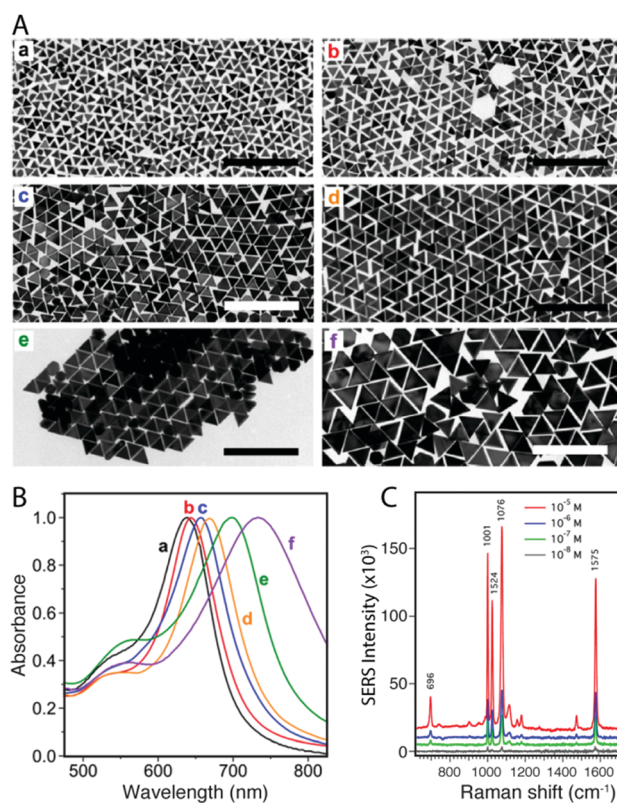
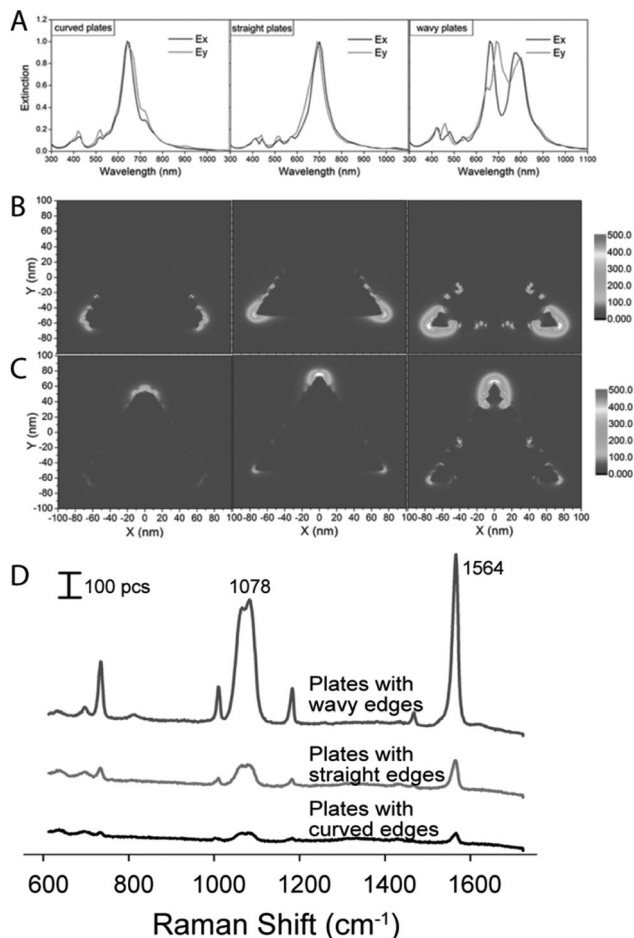


Fig. 9 (A) TEM images of AuNTs with increasing edge lengths from 60 to 150 nm (scale bar 500 nm). (B) UV-Vis spectra of the AuNTs depicted in TEM images (a-f). (C) SERS performance of AuNTs in solution for thiophenol (TP) excited at 785 nm and concentrations varying between  $10^{-5}$  to  $10^{-8}\text{ M}$ . Reproduced with permission of ref. 25 Copyright © 2014 American Chemical Society.



**Fig. 10** (A) Calculated extinction spectra of AgNTs with curved, straight, and wavy edges, using FDTD calculations and with the incident light propagating along the z-axis. (B and C) Electric field amplitude patterns of a NT with electric field along the x-axis ( $E_x$ ) and y-axis ( $E_y$ ), for (B and C) respectively, and an excitation wavelength of 780 nm. (D) Comparison of SERS spectra at 785 nm laser excitation, taken from aqueous suspensions of 1,4-benzenedithiol coated AgNTs with straight, curved, and wavy edges, respectively. Reproduced with permission ref. 26 Copyright © 2013 Wiley-VCH Verlag GmbH & Co.

better match is obtained between incident laser and LSPR, rather than a higher enhancement of the electric field at the wavy edge substructures. The selection of NPs with LSPRs that match the excitation laser is therefore critical. This was also confirmed by Tan *et al.* who synthesized AgNTs of different edge lengths, from 30 up to 210 nm with corresponding LSPR maxima between 485 and 1130 nm.<sup>27</sup> They measured the EF of adenosine triphosphate (ATP) and rhodamine 6G (R6G) with two different laser wavelengths (458 and 633 nm) and observed a close relationship between the EF and the LSPR. The maximum EF (around  $10^4$ – $10^5$ ) was invariably obtained for NTs with LSPR matching the selected laser wavelength and, in analogy to NRS, decreased up to two orders of magnitude for off-resonance wavelengths. At this point it is important to mention that SERS enhancement can also be obtained for off-resonance illumination, where the chemical enhancement of  $10$ – $10^2$  is expected to play an important role. Tiwari *et al.* compared the off-resonance SERS for

AgNPs with different morphologies observing the following enhancement sequence: AgNTs > Ag nanospheres > AgNRs.<sup>28</sup> Since the LSPR maximum for nanospheres was shifted away from the incident wavelength as compared to NRs, they concluded that chemical enhancement played an important role. They also suggest that this effect could be due to the higher abundance of lower activity {111}, and {100} facets in these NRs as compared to Ag nanospheres which expose nearly all fcc crystal facets. It should be noted that this trend is inconsistent with results on the comparison of SERS performance between AuNRs and nanospheres in ref. 18. The reason for such a contradictory result could be related to differences in NRs geometry and the use of different analytes in different concentrations. Often Ag nanospheres show higher polydispersity, more defects and shape deformations (facetting) than Au spheres, which could explain the higher abundance of reactive facets. Another issue is the  $10^{-3}$  M concentration of R6G used with AgNPs. Such high analyte concentrations typically lead to NP aggregation, resulting in extraordinarily intense SERS signals.

## 5. Nanocubes and nanocages

Nanocubes (NCs) are nanostructures composed of six symmetric square faces, each three of them meeting at each vertex (regular hexahedron). In general, for AgNCs it has been easier to obtain higher quality and uniformity than for AuNCs.<sup>29</sup> A standard method to prepare AgNCs comprises the reduction of  $\text{AgNO}_3$  with ethylene glycol, which is used as both solvent and reducing agent. By adding HCl to the reaction mixture, single-crystal AgNCs are obtained, at the expense of longer reaction times. Xia *et al.*<sup>29</sup> presented a sulfide-mediated protocol, with reaction times below 15 min, by including a trace amount of  $\text{Na}_2\text{S}$  to the synthesis. In the presence of ethylene glycol and  $\text{AgNO}_3$ ,  $\text{Ag}_2\text{S}$  nanocrystallites were produced, which then catalyse the reduction of  $\text{AgNO}_3$ . Because of the fast reduction rate, the formation of twinned Ag seeds was limited and the cube shape further promoted. The authors claimed that PVP selectively binds onto {100} Ag facets, thereby facilitating the formation of NPs with cubic shape. The synthesis of monodisperse AuNCs has however been challenging, and key parameters such as reproducibility and fine size control still require further optimization.<sup>30</sup> The most common method is based on seed-mediated growth, in combination with alkyltrimethyl ammonium halide surfactants such as CTAC, CTAB or CPC (cetylpyridinium chloride). The final shape is thus directed by kinetic control, reducing agent (ascorbic acid) concentration and selective absorption of halide ions on certain facets. In addition, crystal habits of the seeds play a key role on the final shape, single crystal seeds being required for cubic structures.

As predicted by Fuchs in 1975 and explained by Cortie *et al.*,<sup>31</sup> the main radiative resonances in a cube are the six distinct modes represented in Fig. 11A, where it can be seen that dipolar LSPR charges tend to accumulate at corner sites (C1 in Fig. 11A). DDA-calculated extinction, absorption, and scattering spectra of a 40 nm AgNC are shown in Fig. 11B, and

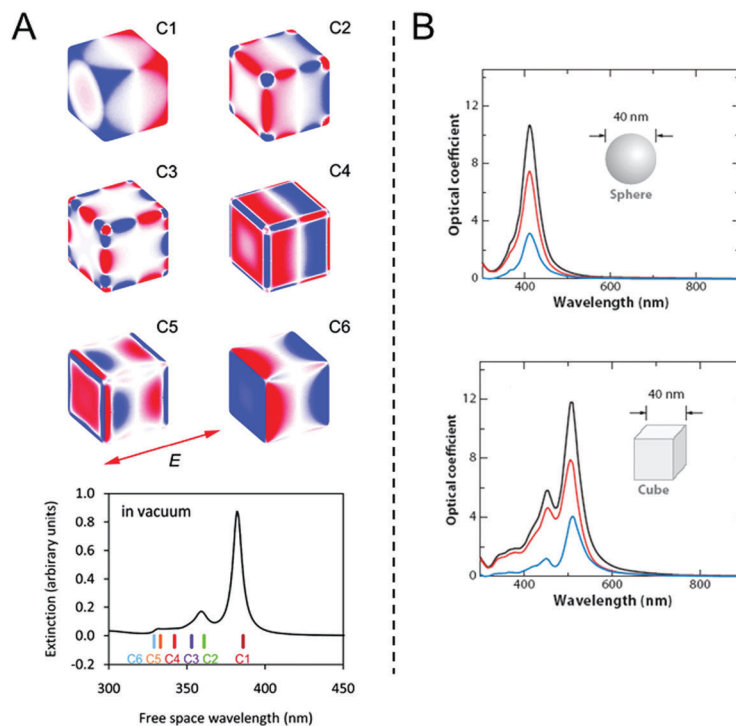


**Fig. 11** (A) Six strongest radiative cube plasmon resonances and the associated optical extinction spectrum simulated using Johnson and Christy dielectric data for Ag in vacuum.<sup>31</sup> (B) Extinction (black), absorption (red), and scattering (blue) spectra calculated for an Ag sphere and an Ag cube.<sup>32</sup> Reproduced with permission of ref. 31 and 32 Copyright © 2006, 2012 American Chemical Society.

compared to those for an Ag nanosphere. More peaks appear in the NCs spectrum due to the distinct symmetries of NC plasmon resonances, and the most intense peak (C1 dipole mode) is red-shifted with respect to the spherical shape.<sup>32</sup> Although the resonances in AgNCs should be quite sharp, this is not easily appreciated experimentally, due to several issues such as polydispersity or surface scattering (damping) of the resonance. Cortie *et al.* also showed that with a sufficient degree of monodispersity in silver right cuboids, at least four pronounced extinction peaks can be visualized.<sup>31</sup> They confirmed that the presence or absence of individual peaks is turned on and off by changes in the refractive index of the surrounding medium, the rounding of corners, or changes in one of the NC dimensions. Recently, AgNCs supported on silicon nitride were analyzed by 3D tomographic reconstruction of EELS maps recorded at different tilt angles. The results showed a significant influence of the substrate, together with the observation of higher order plasmon modes.<sup>33</sup>

Due to the strong LSPR and hotspots highly localized at corners, NCs are excellent candidates as SERS substrates. The importance of sharp tips has been demonstrated by comparing the SERS activity of AgNCs with sharp or truncated corners deposited on silicon substrates, and functionalized with 1,4-benzenedithiol (1,4-BDT).<sup>34</sup> As shown in Fig. 12, variations in SERS intensity were observed depending of the sharpness of the corners and orientation relative to the polarization of the excitation laser. As expected, the angular dependence was less significant when the NCs were truncated and became nearly spherical.

When the SERS response of AuNCs is compared to other symmetric structures such as rhombic dodecahedra and octahedra, differences in the signal intensity were still observed.<sup>35</sup> To avoid any additional interference, all the NPs were covered by CTAC (so equal hindrance was expected for the Raman active molecules to reach the NP surface in all cases), and the experiments were performed at the same nanocrystals concentration and excitation wavelength of 633 nm. The LSPR slightly shifted from particle to particle but all of them were between 550 and 600 nm: octahedral nanocrystals with edge lengths of 53 and 75 nm, and maximum absorption at  $\lambda_{\text{max}} = 570$  and 585 nm; rhombic dodecahedra of 32 and 43 nm,  $\lambda_{\text{max}}$  at 550 and 570 nm; and NCs of 44 nm and 72 nm,  $\lambda_{\text{max}}$  at 550 and 580 nm. In Fig. 13B and C the relative SERS activity of these nanostructures is presented, where the intensities of the  $998 \text{ cm}^{-1}$  Raman shift of thiophenol (TP) from all spectra were collected over the concentration range of  $10^{-5}$  to  $10^{-8}$  M. The results indicate that, 32 nm rhombic dodecahedra ( $\lambda_{\text{max}} = 550$  nm) were the ones with the strongest signal enhancement, reaching a detection limit for TP down to  $10^{-8}$  M. The comparison shows that other shapes such as rhombic dodecahedra can exhibit higher EM, however the synthesis with good reproducibility of AuNPs with these shapes is harder to achieve, therefore much less used in SERS.

Alternative to NCs with flat faces, concave NCs can also be prepared *via* modifications of the seed-mediated-growth method, where CTAC provides control over the concave morphology of the final product. It is well known that certain facets show higher chemical activities than others. In the case shown above, for example, TP has a higher affinity to  $\{110\}$  surface planes due to

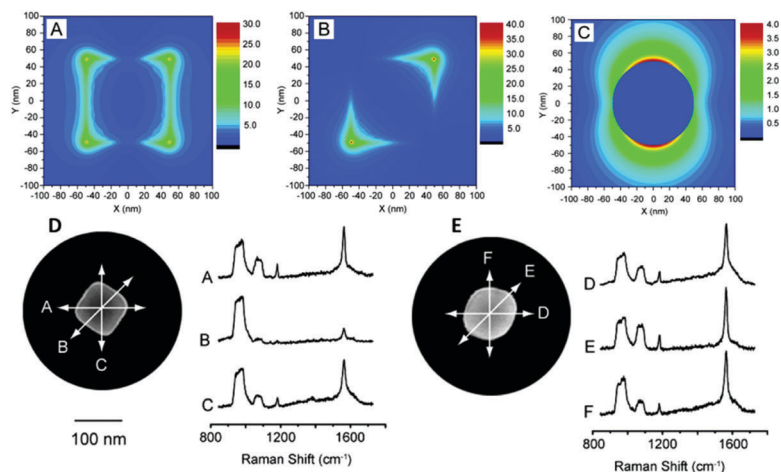


**Fig. 12** EM field amplitude patterns for a 100 nm AgNC at two polarizations, compared to a 100 nm Ag nanosphere when irradiated at 514 nm: (A) 100 nm AgNC, with the incident light along the z-axis and the electric field along the x-axis or [100] direction; (B) 100 nm Ag NC, with the incident light along the z-axis and E-field along the [110] direction. (C) 100 nm Ag nanosphere, with the incident light along the z-axis and electric field along the x-axis. (D and E) Normalized SERS spectra of 1,4-BDT adsorbed on a AgNC with sharp corners (D) and on a highly truncated AgNC (E) at various angles relative to the polarization of the excitation laser. Arrows in SEM images indicate the polarization directions of incident laser corresponding to the spectra. The scale bar applies to both images. The spectra were stacked with off-set for clarity. Reproduced with permission of ref. 34. Copyright © 2007 American Chemical Society.

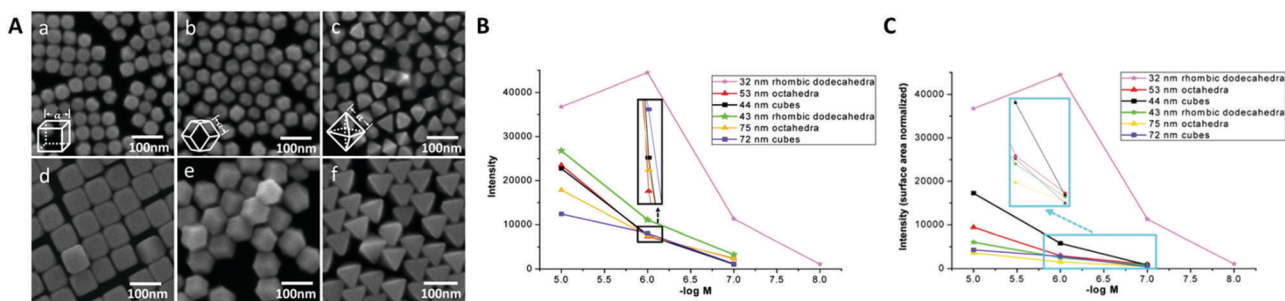


**Fig. 13** (A) SEM images of cubic (a and d), rhombic dodecahedral (b and e), and octahedral (c and f) gold nanocrystals with edge lengths of 44 (a), 32 (b), 53 (c), 72 (d), 43 (e), and 75 (f) nm. (B) SERS intensities of the 998  $\text{cm}^{-1}$  peak versus the negative logarithm of TP concentration in particle solutions. Data points at a  $10^{-6}$  M were expanded to make their relative intensities visible. (C) Intensities of the band at 998  $\text{cm}^{-1}$  (normalized to total particle surface-area) versus the negative logarithm of TP concentration. Reproduced with permission of ref. 35. Copyright © 2013 American Chemical Society.

higher binding energies (33.413  $\text{kcal mol}^{-1}$ ) compared to {111}, {100} (7.742 and 17.498  $\text{kcal mol}^{-1}$ ).<sup>35</sup> Concave NCs display high index facets ({720} facets for Au) with correspondingly higher chemical activities, thereby improving the performance as SERS substrates. Plasmon resonances in concave NCs are in general red-shifted as compared to NCs with flat faces. As concave-NCs have sharper tips than NCs with flat faces, higher EM field enhancements are expected (see Fig. 14), which in turn lead to higher SERS signals. For instance, Romo-Herrera *et al.* compared three NCs with different sizes and increasing concavity. The assayed NCs displayed maximum absorbance at 566, 616 and 692 nm, for small, intermediate and big NCs, respectively. By measuring SERS at two excitation wavelengths of 633 and 785 nm, variations in the EF were studied as a function of size. As expected, the highest EF was achieved for those cases with the best match between LSPR and excitation wavelength (Fig. 14B), namely  $\text{EF} = 1.6 \times 10^6$  for medium Au concave-NCs at 633 nm excitation and  $\text{EF} = 4.2 \times 10^6$  for big Au concave-NCs at 785 nm

excitation.<sup>36</sup> Although the higher enhancement was produced for the more concave structure, with sharper vertices, the differences in size and separation from the excitation wavelength make the results difficult to compare.

Closely related to nanocubes are so-called nanocages (NCg, see TEM images in Fig. 15A–D). AuNCgs are hollow and porous NPs created by galvanic replacement when AgNPs are treated with chloroauric acid in boiling water (note that some Ag is usually left after the process).<sup>29</sup> A distinct property of AuNCgs is that the LSPR bands are red-shifted into the NIR, rendering them particularly useful for biological applications. A comparative study between AgNCs and bimetallic Ag–Au NCgs has demonstrated a strong relationship between excitation wavelength, SERS intensities and Au content in the NCgs.<sup>37</sup> The authors made three important points. (1) Pure AgNCs display the most intense LSPR with the narrowest spectral linewidth and lowest plasmon damping, thereby leading to the highest SERS efficiency regardless of whether excitation was under on- or off-resonance

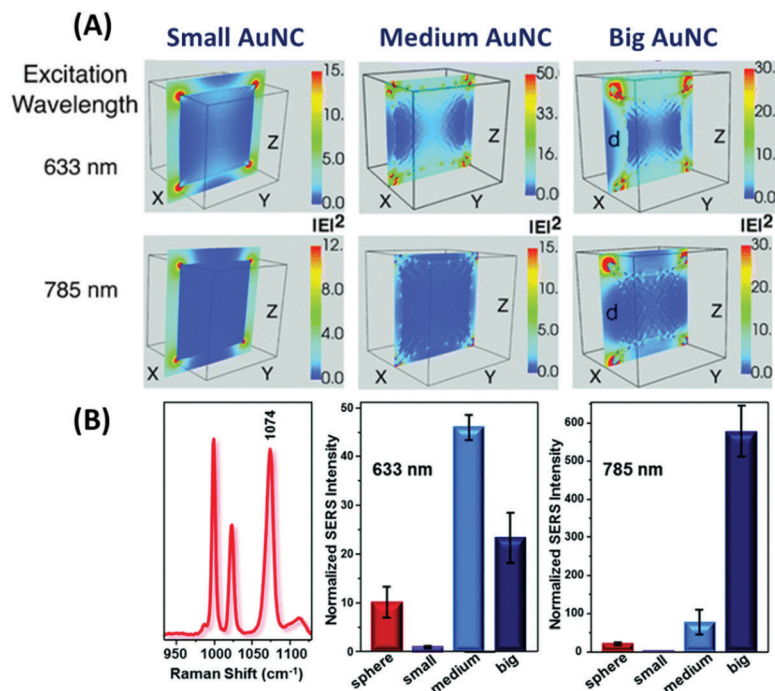


**Fig. 14** (A) DDA calculations of different sizes of AuNCs with different concavity degree. The yz plane cutting in half of an AuNC shows the depth of concavity and its effect on field intensity. (B) Representative SERS spectrum of TP in the 940–1150  $\text{cm}^{-1}$  spectral range and the SERS intensities registered at 1074  $\text{cm}^{-1}$ , upon excitation at 633 nm and 785 nm, for the different AuNCs. Experimental conditions were the same for all samples. Reproduced with permission of ref. 36 Copyright © The Royal Society of Chemistry 2016.

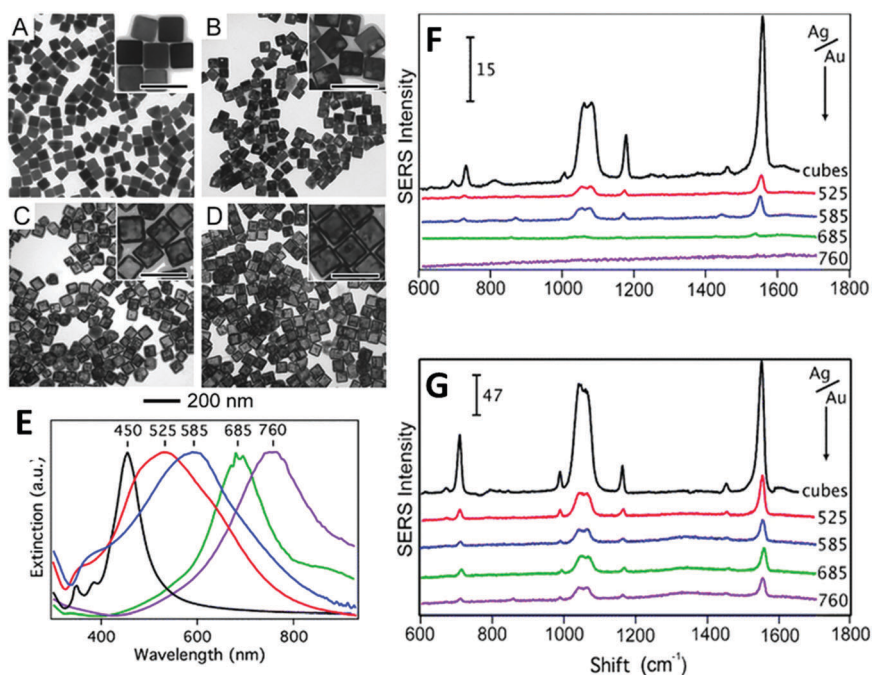


**Fig. 15** (A–D) TEM images of nanocages at degrees of galvanic replacement. (E) UV-Vis-NIR extinction spectra of nanocages varying Au amount (increasing from left to right). (F and G) SERS spectra of 1,4-BDT taken from and NCgs where the wavelength (in nm) next to each spectrum indicates the LSPR for each sample. The spectra in (F) were recorded under 514 nm excitation whereas for those in (G) 785 nm excitation was used. SERS spectra were normalized to account for differences in concentration. The number and scale bar in each graph corresponds to Analog-Digital Units (ADU)  $\text{mW}^{-1} \text{s}^{-1}$ . Reproduced with permission of ref. 37 Copyright © Royal Society of Chemistry 2009.

conditions (Fig. 15E). (2) The SERS performance of bimetallic Ag–Au NCs rapidly decreases with increasing Au content under 514 nm excitation, which matches interband transition energies in Au, leading to effective plasmon damping. The observed behavior is in agreement with the expected trend of signal decrease by LSPR detuning away from excitation wavelength (see Fig. 15E and F). (3) In contrast, under 785 nm excitation (outside of the Au interband transition range), SERS intensity is high for all bimetallic NCs with different Au contents (see Fig. 15G). Interestingly, tuning the LSPR closer to the excitation wavelength did not necessarily result in an increase of the signal intensity.

## 6. Branched nanoparticles – nanostars

Branched NPs – also called nanostars (NSs), nanoflowers or multipods – are NPs formed by a central body and several arms or tips that protrude from it. These branches can be symmetrically distributed, in the case of nano-hexapods or penta-NSs formed by tip protrusion from octahedral or decahedral vertices, respectively. When tips are randomly oriented and shaped, NPs are referred to by the more general term nanostars. In some cases, the tips are not only irregular but can even be hyperbranched forming dendritic shapes and increasing the number of arms in non-radial directions.

A number of synthetic methods based on wet chemistry have been reported for the preparation of branched nanoparticles, especially for AuNSs, but also for Ag and other noble metals.<sup>38</sup> Both seed-mediated growth and one-pot methods are currently available, the former generally leading to higher uniformity (monodispersity). To cite just a few examples, branched gold NPs were obtained through seed-mediated growth by reduction of HAuCl<sub>4</sub> with ascorbic acid, in the presence of CTAB or CTAC surfactants and addition of AgNO<sub>3</sub>; but also in surfactant-free synthesis with the addition of AgNO<sub>3</sub>; using *N,N*-dimethylformamide (DMF) as solvent and reducing agent in the presence of PVP; or *via* one-pot synthesis in HEPES buffer. Template-based methods have also been used in which radial mesoporous silica covering a gold core was used to guide the growth of gold tips. Prominent examples of the synthesis of Ag branched NPs include seed-mediated growth with sodium polyacrylate and decahedral seeds; two-step reduction of AgNO<sub>3</sub> by hydroxylamine and citrate; and the reduction of AgNO<sub>3</sub> by *L*-ascorbic acid – in this case the branching mechanism is attributed to aggregation of discrete nanoparticles facilitated by ascorbic acid.

The characteristic morphology of NSs confers them with ideal optical response toward applications such as LSPR and SERS sensing. The UV-Vis-NIR spectra of AuNSs typically feature a plasmon band in the 600–1200 nm region, corresponding to plasmon modes confined at the tips, as well as a smaller band/shoulder around 500–600 nm, related to a mode localized at the central body. LSPR in AuNSs can be tuned through changes in the tips sharpness and/or AR. Red-shifts are observed when the tip AR increases, similar to NRs (Fig. 16A).<sup>39</sup> In general, larger

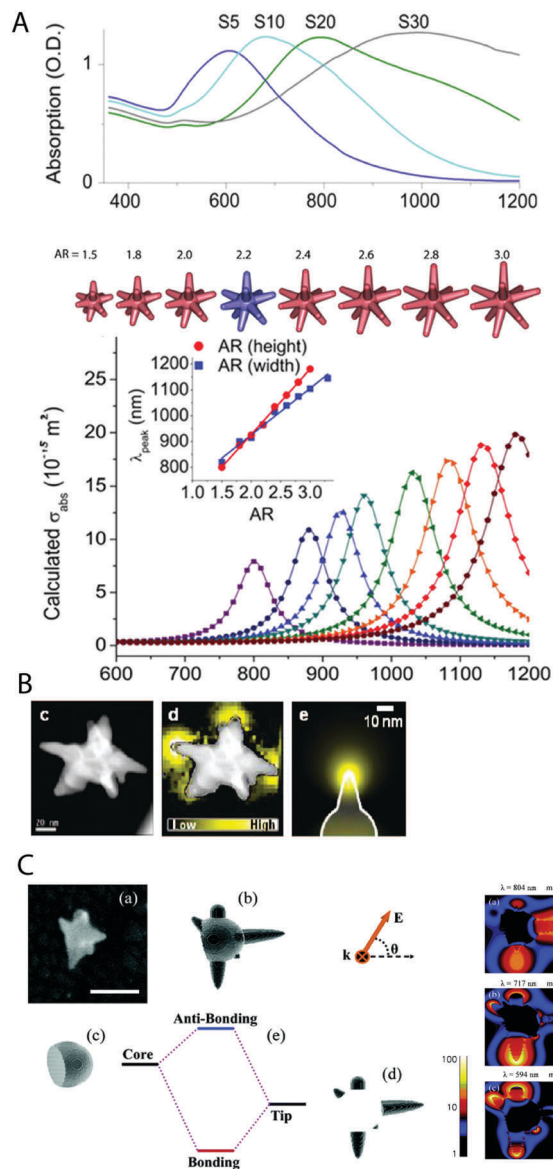


**Fig. 16** (A) Optical properties of AuNSs with different branching degrees. An increase in branching produces a red-shift in the corresponding spectra. This is also shown in calculated spectra obtained by BEM by changing the tips AR.<sup>39</sup> (B) HAADF-STEM image of a gold nanostar, overlapping EELS mapping showing the enhancement for tips plasmon modes, and calculated BEM image of a model 1-tip nanostar.<sup>42</sup> (C) SEM image of a AuNS and the corresponding model (scale bar: 100 nm). Plasmon mode hybridization is sketched in the scheme and calculated EM field enhancements (FDTD), are shown as a function of polarization and wavelength of the excitation light.<sup>41</sup> Reproduced with permission of: ref. 39 Copyright © IOP Publishing 2012; ref. 41 and 42 Copyright © American Chemical Society 2007 and 2009.

NSs display an increased number and longer tips, in correlation with an LSPR red-shift as the size increases. EELS mapping of AuNS together with BEM simulations revealed an extremely high EM field enhancement at the tips, corresponding to a low energy dipolar plasmon mode (Fig. 16B).<sup>40</sup> On the basis of single particle UV-Vis spectroscopy and FDTD calculations, Nordlander and co-workers proposed that plasmon modes in NSs actually arise from hybridized modes from coupling between

the tips and the central body (Fig. 16C).<sup>41</sup> Such a plasmon mode hybridization produces an antenna effect resulting in EM field enhancement of up to 4 times the one that would be exclusively produced by the tips. In addition, due to the polydispersity in tip shape and orientation, plasmon bands from AuNS colloids are usually broader than those for NRs, thereby facilitating the use of Raman excitation lasers that do not precisely match the absorbance maximum, but are still on-resonance with a significant proportion of plasmon modes.

Branched nanoparticles display particularly high EFs at the resonance wavelength, even higher than those for rod or sphere dimers,<sup>44</sup> thus enabling unprecedentedly low detection limits for single particles. Rodríguez-Lorenzo *et al.* achieved zeptomole detection limits when AuNSs were used to measure 1,5-naphthalene-dithiol (1,5-NDT) that was located between a Au substrate and a AuNS tip covalently bonded to both surfaces.<sup>42</sup> In this case, an additional enhancement was obtained due to the plasmon coupling between the flat Au substrate and the NS tip, thereby creating a hotspot with even higher SERS enhancement. Indrasekara *et al.* used AuNSs on a deposited substrate (Fig. 17A) to detect 4-mercaptobenzoic acid (4-MBA) with limits of detection as low as 10 fM, corresponding to enhancement factors of  $10^9$ .<sup>43</sup> The authors also compared three different AuNS sizes with plasmon bands around 800, 700 and 600 nm (for large, intermediate and small NSs, respectively), and obtained enhancement factors of  $4.9 \times 10^9$ ,  $1.6 \times 10^9$ , and  $5.3 \times 10^8$ , respectively,

when illuminating at 785 nm (Fig. 17C and D). As expected, the EFs correlated with the proximity between the resonance frequency and the excitation laser. When the authors used nanospheres instead of NSs, EFs of only  $10^4$  to  $10^5$  were obtained. It is worth mentioning that, despite of NSs being deposited on a substrate, a further increase of SERS enhancement is not expected for dense AuNSs arrays, as recently demonstrated by Solís *et al.* using numerical simulations based on SIE-MoM.<sup>45</sup> They observed a relatively constant enhancement with increasing surface coverage due to the initially high number of intrinsic hotspots in AuNSs and damping in the case of valley to tip contacts. This trend was radically different for nanospheres and NRs, where an increase of coverage resulted in a dramatic increase of enhancement, close to three orders of magnitude. Despite this increase in EF, the order of enhancement was still NSs > NRs > nanospheres when illuminating at the maximum extinction wavelength. It should be noted however, that for NTs the opposite effect has been experimentally observed, with better performance in solution than for a deposited monolayer.<sup>25</sup>

The effect of NS size on SERS enhancement has been addressed by Khoury *et al.*, using an illumination wavelength far away from the LSPR maximum, and taking advantage of the breadth of AuNS plasmon bands.<sup>47</sup> They synthesized PVP-coated AuNSs with 6 different sizes (from 45 to 116 nm) by varying the seeds to HAuCl<sub>4</sub> ratio during the synthesis, resulting in increased number and length of tips, as well as an LSPR red-shift

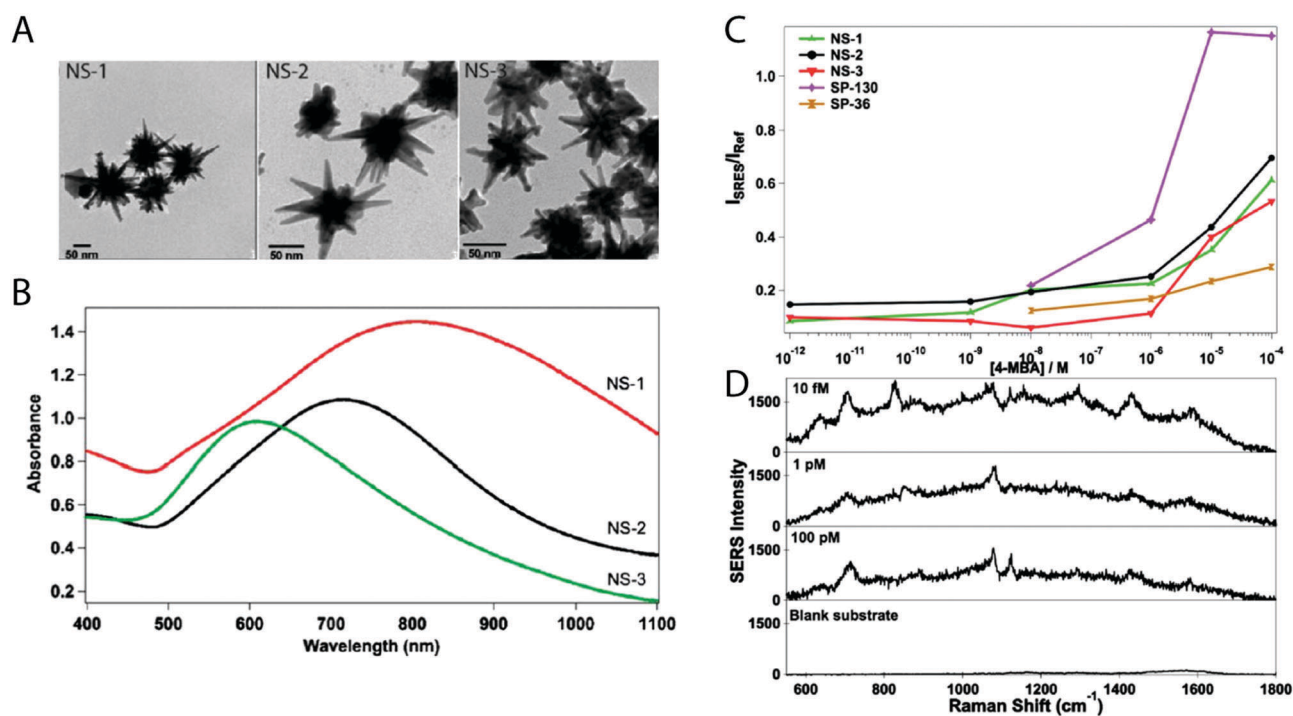


Fig. 17 (A) TEM image of AuNSs synthesized with three different sizes. (B) Absorbance spectra of the corresponding NSs of (A) tested in SERS detection. (C) Quantitative SERS analysis facilitated by the SERS substrates (three different NSs and two spherical NPs), with varying 4-MBA concentration and represented as the relative intensity at the  $1077 \text{ cm}^{-1}$  peak. Below  $10^{-8} \text{ M}$  no signal could be detected for the nanospheres (incident laser was 785 nm for NSs and 633 nm for nanospheres). (D) Characteristic SERS spectra of 4-MBA at different concentrations. Reproduced with permission of ref. 43 Copyright © Royal Society of Chemistry 2014.

(from  $\sim 700$  to  $\sim 850$  nm). EFs around  $5 \times 10^3$  were achieved for 4-MBA, but no big differences were observed among the different sizes, probably due to a similar chemical enhancement, and absorbance off-resonance with respect to the illumination. Note that EF values obtained from different works are not fully comparable (see above), since parameters such as concentration, NP coatings, or SERS substrate preparation play an important role in the final values. One of the few examples where NP shapes were compared in solution involved AuNSs, NTs and nanospheres of similar sizes, as well as small nanosphere aggregates (Fig. 18).<sup>46</sup> They found that SERS of R6G was negligible for nanospheres with a resonance peak at 532 nm, when compared to other shapes. Upon aggregation, the nanospheres displayed a red-shifted LSPR at 660 nm, while NTs and NSs peaked at 800 and 785 nm, respectively. Using R6G as the analyte and exciting at 785 nm, the resulting SERS enhancement sequence was: nanosphere aggregates < NTs < NSs, which was attributed to the increase of hotspots and the magnitude of LSPR absorbance at the excitation wavelength. However, differences in organic coating and zeta potential between the different particles, which may obviously affect the adsorption of the organic dye on the NP cores, cannot be discarded as a potential source of SERS variation.

## 7. More complex systems

Although the morphologies discussed above (NRS, NTs, NCs, and NSs) are by far the most frequently used anisotropic NP shapes for SERS sensing, many other shapes containing intrinsic hotspots have been or could potentially be used. These include, *e.g.* regular or highly symmetric shapes such as octahedra, decahedra and bipyramids, as well as a myriad of other irregular shapes containing intrinsic hotspots at sharp edges or tips. Additionally, the anisotropic morphology of NPs not containing intrinsic hotspots could still be advantageously used in certain cases, whereas extrinsic hotspots can be generated by means of directed assembly strategies. This is the case for nanoshells, where the core-shell configuration (dielectric core@metallic shell) allows LSPR tuning into the red or NIR regions, where illumination is most appropriate for biological applications. Hotspots have been created with these NPs *via* formation of monolayers, resulting in NP-NP and NP-substrate hotspots.

Anisotropy in NPs can also be used to solve the specific requirements for detection in a complex system. Uji-i and co-workers devised a strategy by which an AgNW could be used for so-called SERS endoscopy, penetrating inside a living cell and probing the chemical composition at different locations by SERS.<sup>48</sup> The AgNW (50 nm in diameter) was attached to a tungsten tip used for micromanipulation and two different NW excitation methods were used: directly at the NW tip and far away from the tip (remote excitation SERS or RE-SERS), making use of the propagation of surface plasmon polaritons along the AgNW (Fig. 19A). These authors recorded a higher signal inside the cell nucleus, due to the presence of DNA and proteins, as compared to the cytoplasm (a more crowded environment) or the buffer at the cell exterior (Fig. 19B). Interestingly, a much clearer

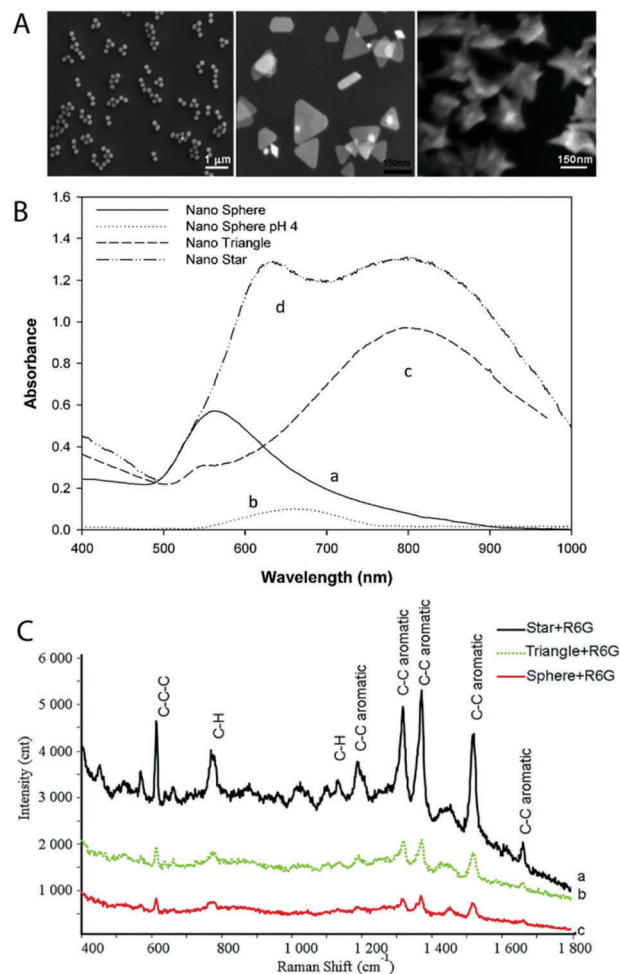


**Fig. 18** Influence of gold nanoparticle shape on SERS enhancement. (A) Scanning electron microscopy images of NPs with different morphologies: aggregated nanospheres, NTs and NSs. (B) UV-Vis spectra from the different nanoparticles at constant NP concentration ( $N = 6 \times 10^8$  particles per mL). (C) SERS spectra from 5  $\mu$ M R6G, using nanoparticles of different shapes ( $3 \times 10^9$  particles per mL,  $\lambda_0 = 785$  nm). Reproduced with permission of ref. 46 Copyright © Royal Society of Chemistry 2014.

signal was obtained for the RE-SERS measurement (Fig. 19G), which was attributed to lower cell damage (and therefore lower toxicity), as well as a lower amount of stacked molecules at the AgNW tip.

Interestingly, not only nanoparticle anisotropy could be useful to solve specific problems, but a combination of anisotropic metal NPs with different materials can result in probes with superior features. Fales *et al.* showed that, upon partial coverage of a AuNS with Ag, the SERS signal could be increased up to one additional order of magnitude.<sup>49</sup> Ag coating occurred mainly on the AuNS core and the maximum SERS signal was achieved for the highest coating that still left the Au tips free. This enhancement in AuNSs@Ag was attributed to the remaining AuNS hotspots, while the NP plasmon was shifted towards an off-resonance situation, which decreased self-absorption. The authors further covered the NPs with a silica shell (AuNS@Ag@SiO<sub>2</sub>), thereby trapping the dye reporter at the NP surface and

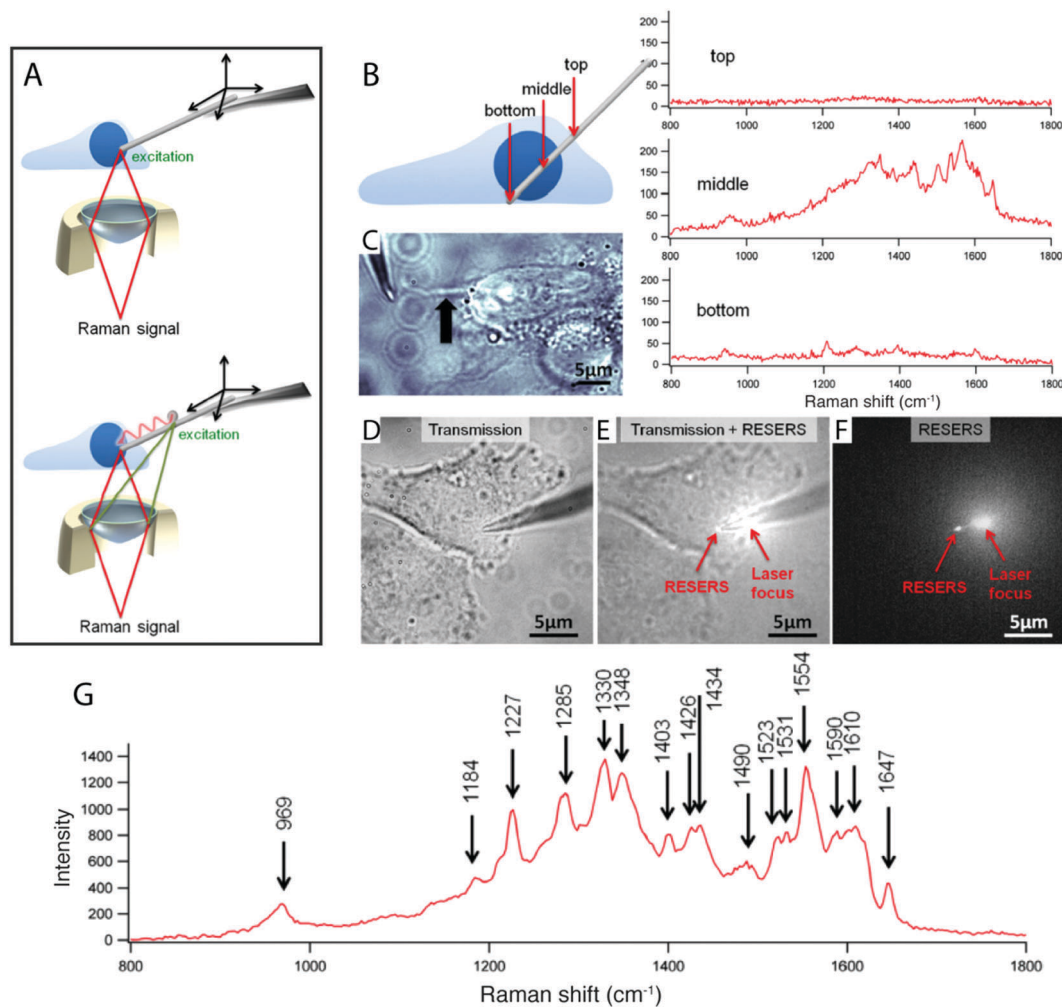


**Fig. 19** SERS endoscopy of a living cell using an AgNW. (A) Schematic illustrations of plasmonic waveguide SERS endoscopy using an AgNW in direct and remote excitation modes, (top and bottom cartoons, respectively). (B) Scheme of the positions chosen for direct excitation SERS spectroscopy inside a live HeLa cell during AgNW probe endoscopy, and corresponding SERS spectra (the HBSS buffer, the cell nucleus, and the cell cytoplasm). (C) After direct excitation SERS endoscopy measurement, cell components adhere to the AgNW probe and come out with the probe during release (indicated by the arrow). (D–F) Images of an AgNW probe using RE-SERS endoscopy of a live HeLa cell, by optical transmission (D), combination of optical transmission and RE-SERS (E) and RE-SERS only (F). (G) RE-SERS spectrum from the nucleus of a live HeLa cell. Reproduced with permission of ref. 48 Copyright © Wiley-VCH Verlag GmbH & Co. 2014.

making the signal less sensitive to other molecules, which was proposed as a suitable probe for SERS bioimaging. Another example of composite NPs was demonstrated by Reguera *et al.*, who prepared Janus magnetic nanostars (JMNSs) comprising an asymmetric AuNS attached to an epitaxially attached iron oxide nanosphere. Such multifunctional NPs could be used as SERS substrates, allowing magnetic concentration of NP and analyte, thereby increasing the Raman signal.<sup>50</sup> Fig. 20A shows an electron tomography image of one such nanostructure, where the Janus configuration of AuNS and iron oxide NP can be clearly appreciated, allowing selective functionalization of both components. These NPs were used to measure crystal violet (CV) in solution, at a sub-micromolar concentration (Fig. 20C in red). Interestingly, a 5-fold increased enhancement was recorded when a hand-held magnet was used to concentrate the NPs after incubation with the analyte (Fig. 20C, blue lines).

By using this strategy, it was possible to detect CV concentrations down to 15 nM, well below the limit of detection in solution. Therefore, the NPs could be used to improve the “capture” of analyte in solution (small diffusion distances) prior to magnetic concentration, producing a local accumulation of the analyte at the spot where the Raman excitation laser was focused.

Although more complex systems are being developed to solve particular problems, or with higher sensitivity, there is also a need to develop quantitative and reliable SERS. For the case of anisotropic nanoparticles this includes the intra- and inter-lab reproducibility of samples, the stability of the substrates and a reliable calibration. Although this analysis is out of the scope of the current review, many articles have tackled this topic in recent years for different analytes and systems, contributing to the advancement in the use of the technique.

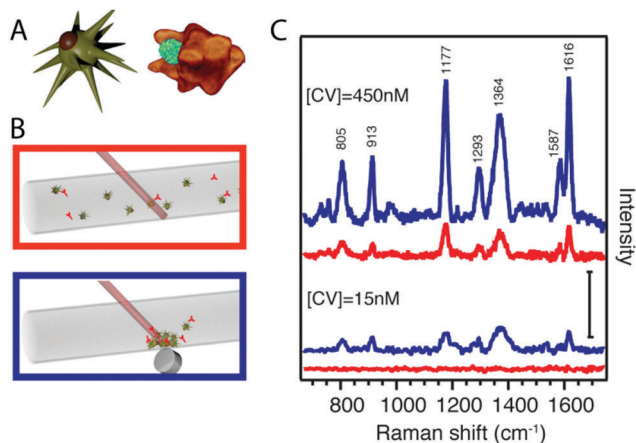


Fig. 20 SERS detection using JMNSs. (A) Schematic representation of the nanoparticle morphology (on the left) and electron tomography image (HAADF-STEM + EDX) of the Janus hetero-NP. (B) Diagram showing the SERS measurement in solution and after magnetic separation of NPs with “trapped” analyte molecules. (C) SERS spectra of CV-containing JMNSs in solution (red) and after magnetic concentration (blue) for two different dye concentrations [CV] = 450 nM (upper spectra) and [CV] = 15 nM (lower spectra). Concentration of JMNSs was [Au<sup>0</sup>] = 0.2 and 0.1 mM, respectively. The spectra were shifted vertically for clarity, the scale bar corresponds to an intensity of 200 counts. Reproduced with permission of ref. 50 Copyright © Royal Society of Chemistry 2014.

## 8. Conclusions

NP synthesis is blooming into plenty of new anisotropic morphologies of mono- and multi-component materials. Better protocols have been designed that produce NPs with high uniformity and yield. Modern Raman instruments provide higher sensitivities and versatility, lower cost, higher portability, *etc.* All these rapid advances offer a promising future for SERS detection in fields where analytes of diverse nature are to be detected. In this situation of high interest on SERS the availability of anisotropic morphologies is a clear advantage toward obtaining ultrasensitive detection and to the design of *ad hoc* configurations that allow the detection of the selected analytes in complex environments such as those in biological or environmental disciplines.

In this tutorial review, we highlighted several comparative works that help elucidating the key morphological parameters to achieve high EFs for SERS. The highest impact on SERS performance comes from the effective near-field enhancement which is in general achieved when the plasmon oscillation is minimally damped, the LSPR wavelength matches the excitation wavelength (on-resonance condition) and the NP exhibits preferentially a large number of protrusions with high curvature giving rise to highest polarizability. The importance of LSPR efficiency regarding plasmon damping becomes evident when comparing Au and Ag NPs. An additional chemical effect favors the application of anisotropic NPs because of the presence of highly reactive facets with higher binding affinities for analytes as compared to nanospheres.

However, an overall evaluation of the NPs as SERS substrates, *e.g. via* EF is not simple due to the difficulties of controlling

certain parameters such as the type and quality of organic coatings or limitations regarding the available laser wavelengths. The evaluation is even more complicated when EFs are compared among different laboratories, where the lack of standardized protocols makes it virtually impossible. Many factors influence the SERS output, the establishment of such procedures and standardization are absolutely desirable, and within the rising commercial interest of NPs for SERS it will be indispensable. Besides the confinement and strength of the local EM field and the material, the surface chemical sensitivity of SERS results in parameters such as nature of the analyte, the chemical affinity to the nanoparticle surface, concentration of NP and analyte (or the ratio of both), surface coverage, coating/protection layer *etc.* playing important roles. Further, the stability of the analyte-NP ensemble under given conditions should be taken into account. On one hand, the interplay among these factors offers plentiful possibilities but at same time a rational design of the NP for a specific application is often required and limits the generalization of the SERS substrate.

## Acknowledgements

This work has been funded by the European Research Council (ERC Advanced Grant #267867, Plasmaquo).

## References

- 1 K. L. Kelly, E. Coronado and L. L. Zhao, *J. Phys. Chem. B*, 2003, **107**, 668–677.
- 2 P. K. Jain, K. S. Lee, I. H. El-Sayed and M. A. El-Sayed, *J. Phys. Chem. B*, 2006, **110**, 7238–7248.
- 3 M. Fleischmann, P. J. Hendra and A. J. McQuillan, *Chem. Phys. Lett.*, 1974, **26**, 163–166.
- 4 L. Sun, P. Chen and L. Lin, in *Applications of Molecular Spectroscopy to Current Research in the Chemical and Biological Sciences*, ed. M. T. Stauffer, InTech, 2016, pp. 383–404.
- 5 Z. Yong, D. Y. Lei, C. H. Lam and Y. Wang, *Nanoscale Res. Lett.*, 2014, **9**, 187.
- 6 M. Li, S. K. Cushing, J. Zhang, J. Lankford, Z. P. Aguilar, D. Ma and N. Wu, *Nanotechnology*, 2012, **23**, 115501.
- 7 N. C. Lindquist, P. Nagpal, K. M. McPeak, D. J. Norris and S.-H. Oh, *Rep. Prog. Phys.*, 2012, **75**, 036501.
- 8 E. C. Le, Ru, E. Blackie, M. Meyer and P. G. Etchegoin, *J. Phys. Chem. C*, 2007, **111**, 13794–13803.
- 9 H. Chen, L. Shao, Q. Li and J. Wang, *Chem. Soc. Rev.*, 2013, **42**, 2679–2724.
- 10 N. R. Jana, L. Gearheart and C. J. Murphy, *Chem. Commun.*, 2001, 617–618.
- 11 B. Nikoobakht and M. A. El-Sayed, *Chem. Mater.*, 2003, **15**, 1957–1962.
- 12 X. Ye, C. Zheng, J. Chen, Y. Gao and C. B. Murray, *Nano Lett.*, 2013, **13**, 765–771.
- 13 A. Sánchez-Iglesias, N. Winckelmans, T. Altantzis, S. Bals, M. Grzelczak and L. M. Liz-Marzán, *J. Am. Chem. Soc.*, 2017, **139**, 107–110.

- 14 S. Wang, W. Xi, F. Cai, X. Zhao, Z. Xu, J. Qian and S. He, *Theranostics*, 2015, **5**, 251–266.
- 15 M.-W. Chu, V. Myroshnychenko, C. H. Chen, J.-P. Deng, C.-Y. Mou and F. J. García de Abajo, *Nano Lett.*, 2009, **9**, 399–404.
- 16 B. S. Guiton, V. Iberi, S. Li, D. N. Leonard, C. M. Parish, P. G. Kotula, M. Varela, G. C. Schatz, S. J. Pennycook and J. P. Camden, *Nano Lett.*, 2011, **11**, 3482–3488.
- 17 C. J. Orendorff, L. Gearheart, N. R. Jana and C. J. Murphy, *Phys. Chem. Chem. Phys.*, 2006, **8**, 165–170.
- 18 B. Nikoobakht, J. Wang and M. A. El-Sayed, *Chem. Phys. Lett.*, 2002, **366**, 17–23.
- 19 M. A. Mahmoud and M. A. El-Sayed, *J. Phys. Chem. Lett.*, 2013, **4**, 1541–1545.
- 20 K.-Q. Lin, J. Yi, S. Hu, B.-J. Liu, J.-Y. Liu, X. Wang and B. Ren, *J. Phys. Chem. C*, 2016, **120**, 20806–20813.
- 21 S. T. Sivapalan, B. M. DeVetter, T. K. Yang, T. van Dijk, M. V. Schulmerich, P. S. Carney, R. Bhargava and C. J. Murphy, *ACS Nano*, 2013, **7**, 2099–2105.
- 22 J. Nelayah, M. Kociak, O. Stéphan, F. J. García de Abajo, M. Tencé, L. Henrard, D. Taverna, I. Pastoriza-Santos, L. M. Liz-Marzán and C. Colliex, *Nat. Phys.*, 2007, **3**, 348–353.
- 23 A. Losquin, L. F. Zagonel, V. Myroshnychenko, B. Rodríguez-González, M. Tencé, L. Scarabelli, J. Förstner, L. M. Liz-Marzán, F. J. García de Abajo, O. Stéphan and M. Kociak, *Nano Lett.*, 2015, **15**, 1229–1237.
- 24 A. Brioude and M. P. Pileni, *J. Phys. Chem. B*, 2005, **109**, 23371–23377.
- 25 L. Scarabelli, M. Coronado-Puchau, J. J. Giner-Casares, J. Langer and L. M. Liz-Marzán, *ACS Nano*, 2014, **8**, 5833–5842.
- 26 Y. Yang, X. L. Zhong, Q. Zhang, L. G. Blackstad, Z. W. Fu, Z.-Y. Li and D. Qin, *Small*, 2014, **10**, 1430–1437.
- 27 T. Tan, C. Tian, Z. Ren, J. Yang, Y. Chen, L. Sun, Z. Li, A. Wu, J. Yin and H. Fu, *Phys. Chem. Chem. Phys.*, 2013, **15**, 21034–21042.
- 28 V. S. Tiwari, T. Oleg, G. K. Darbha, W. Hardy, J. P. Singh and P. C. Ray, *Chem. Phys. Lett.*, 2007, **446**, 77–82.
- 29 S. E. Skrabalak, L. Au, X. Li and Y. Xia, *Nat. Protoc.*, 2007, **2**, 2182–2190.
- 30 M. N. O'Brien, M. R. Jones, K. A. Brown and C. A. Mirkin, *J. Am. Chem. Soc.*, 2014, **136**, 7603–7606.
- 31 M. B. Cortie, F. Liu, M. D. Arnold and Y. Niidome, *Langmuir*, 2012, **28**, 9103–9112.
- 32 B. J. Wiley, S. H. Im, Z.-Y. Li, J. McLellan, A. Siekkinen and Y. Xia, *J. Phys. Chem. B*, 2006, **110**, 15666–15675.
- 33 O. Nicoletti, F. de la Peña, R. K. Leary, D. J. Holland, C. Ducati and P. A. Midgley, *Nature*, 2013, **502**, 80–84.
- 34 J. M. McLellan, Z.-Y. Li, A. R. Siekkinen and Y. Xia, *Nano Lett.*, 2007, **7**, 1013–1017.
- 35 H.-L. Wu, H.-R. Tsai, Y.-T. Hung, K.-U. Lao, C.-W. Liao, P.-J. Chung, J.-S. Huang, I.-C. Chen and M. H. Huang, *Inorg. Chem.*, 2011, **50**, 8106–8111.
- 36 J. M. Romo-Herrera, A. L. González, L. Guerrini, F. R. Castiello, G. Alonso-Nuñez, O. E. Contreras and R. A. Alvarez-Puebla, *Nanoscale*, 2016, **8**, 7326–7333.
- 37 M. Rycenga, K. K. Hou, C. M. Copley, A. G. Schwartz, P. H. C. Camargo and Y. Xia, *Phys. Chem. Chem. Phys.*, 2009, **11**, 5903.
- 38 A. Guerrero-Martínez, S. Barbosa, I. Pastoriza-Santos and L. M. Liz-Marzán, *Curr. Opin. Colloid Interface Sci.*, 2011, **16**, 118–127.
- 39 H. Yuan, C. G. Khoury, H. Hwang, C. M. Wilson, G. A. Grant and T. Vo-Dinh, *Nanotechnology*, 2012, **23**, 075102.
- 40 P. S. Kumar, I. Pastoriza-Santos, B. Rodríguez-González, F. Javier García de Abajo and L. M. Liz-Marzán, *Nanotechnology*, 2007, **19**, 015606.
- 41 F. Hao, C. L. Nehl, J. H. Hafner and P. Nordlander, *Nano Lett.*, 2007, **7**, 729–732.
- 42 L. Rodríguez-Lorenzo, R. A. Alvarez-Puebla, I. Pastoriza-Santos, S. Mazzucco, O. Stéphan, M. Kociak, L. M. Liz-Marzán and F. J. García de Abajo, *J. Am. Chem. Soc.*, 2009, **131**, 4616–4618.
- 43 A. S. D. S. Indrasekara, S. Meyers, S. Shubeita, L. C. Feldman, T. Gustafsson and L. Fabris, *Nanoscale*, 2014, **6**, 8891–8899.
- 44 R. Alvarez-Puebla, L. M. Liz-Marzán and F. J. García de Abajo, *J. Phys. Chem. Lett.*, 2010, **1**, 2428–2434.
- 45 D. M. Solís, J. M. Taboada, F. Obelleiro, L. M. Liz-Marzán and F. J. García de Abajo, *ACS Photonics*, 2017, **4**, 329–337.
- 46 F. Tian, F. Bonnier, A. Casey, A. E. Shanahan and H. J. Byrne, *Anal. Methods*, 2014, **6**, 9116–9123.
- 47 C. G. Khoury and T. Vo-Dinh, *J. Phys. Chem. C*, 2008, **112**, 18849–18859.
- 48 G. Lu, H. De Keersmaecker, L. Su, B. Kenens, S. Rocha, E. Fron, C. Chen, P. Van Dorpe, H. Mizuno, J. Hofkens, J. A. Hutchison and H. Uji-i, *Adv. Mater.*, 2014, **26**, 5124–5128.
- 49 A. M. Fales, H. Yuan and T. Vo-Dinh, *J. Phys. Chem. C*, 2014, **118**, 3708–3715.
- 50 J. Reguera, D. Jiménez de Aberasturi, N. Winckelmans, J. Langer, S. Bals and L. M. Liz-Marzán, *Faraday Discuss.*, 2016, **191**, 47–59.